Trigger Level Analysis

Andrew James Strange

School of Physics and Astronomy

The University of Manchester

2017 September

A thesis submitted to the University of Manchester
for the degree of Master of Science
in the Faculty of Engineering and Physical Sciences

Summary

Here is my template for PhD or other theses, for pdfLaTeX (or LaTeX, but pdfLaTeX provides better internal hyperlinks).

It is based on the 'memoir' LaTeX class, which has a lot of useful features/options built-in. The documentation for the memoir class says that '[it] provides the functionality of over thirty of the more popular packages, thus simplifying document sources'.

If there is any specific typesetting feature you want to use in your thesis, you should first check in the comprehensive manual for the memoir class via the link above (which has a detailed index). It may well be that what you want is already provided by the memoir class (and it is better to use its built-in capabilities, rather than loading additional style files, unless you have to).

The rest of this template show various examples of features available.

See `http://www.mrao.cam.ac.uk/~dag/THESIS/` for the current version of this template. (This version is V1.12, dated 2016 September).

Contents

Declaration

This is the declaration. This is not too long, honest!

Acknowledgements

These are the acknowledgements.

-

Chapter 1

Theory

1.1 Standard Model

The Standard Model (SM) of particle physics is a collection of several theories that provides the most accurate theoretical framework for describing all known components of matter and their interactions to date. The model describes three fundamental forces that control interactions between the constituents, each force mediated by an integer spin particle called a *gauge boson*, and the spin-$\frac{1}{2}$ *quarks* and *leptons* that compose all matter. The framework is comprised of quantum field theories where each particle is an excitation of a corresponding field, and the interactions of the fields govern the particle interactions. The mathematical structure is based on the symmetry group $SU(3)_c \times SU(2)_L \times U(1)_Y$ and is required to be gauge-invariant. The SM does not include gravity as gravitational interactions are significantly weaker than the other fundamental forces, so are neglected in this thesis.

wording here? of neglected?

1.1.1 Fermions

The full set of spin-$\frac{1}{2}$ *fermions*, described in Tables 1.1 and 1.2, is the combination of the quark and lepton families, which each have three generations of particle. For each distinct particle there is also an anti-particle which is identical aside from opposite charge and handedness. Most observable matter is made up of solely the first generation of the up and down quarks, the electron and the electron neutrino. Both the leptons and the quarks obey Fermi-Dirac statistics, with quarks experiencing all three fundamental forces, charged leptons interacting via the electromagnetic and weak interactions and neutral leptons experiencing only the weak interaction.

Table 1.1: Spin-$\frac{1}{2}$ fermions: quarks q [1]

Generation	Flavour	Charge / e	Mass / GeV
1	Up u	+2/3	0.002
	Down d	-1/3	0.005
2	Charm c	+2/3	1.28
	Strange s	-1/3	0.096
3	Top t	+2/3	173.1
	Bottom b	-1/3	4.18

Table 1.2: Spin-$\frac{1}{2}$ fermions: leptons l [1]

Generation	Flavour	Charge / e	Mass / MeV
1	Electron e	-1	0.511
	Electron Neutrino ν_e	0	~0
2	Muon μ	-1	105.658
	Muon Neutrino ν_μ	0	~0
3	Tau τ	-1	1776.86
	Tau Neutrino ν_τ	0	~0

To do: Kinda want these side by side, also debating neutron mass

Quarks are always confined into colour singlet hadrons bound by the strong interaction, which are either *baryons* (qqq) or *mesons* ($q\bar{q}$), like the *proton* (uud) and *neutron* (ddu). When a high energy hadron is produced, the interaction of the strong force on the quarks results is a collimated *jet* of hadrons that freeze out of the initial hadron.

1.1.2 Forces

All forces arise due the exchange of unobservable virtual particles, gauge bosons, which obey Bose-Einstein statistics. The three fundamental particle interactive forces for the SM are named the strong, weak and electromagnetic interactions, and are mediated by gluons, weak bosons and photons respectively. The gauge bosons are described in more detail in Table 1.3. In addition to the forces, particles acquire mass by coupling to the Higgs field via the spin-0 Higgs boson [2–4], which is covered in more detail in Section 1.1.3.

To do: undecided on the strength column and numbers withinm which were pulled from undergrad notes

Table 1.3: Spin-1 gauge bosons. The strength of the interaction is typical stated in terms of α, a dimensionless constant proportional to the matrix element for the virtual particle exchange for each interaction. The weak interaction is intrinsically stronger than the EM interaction, but the mass of the weak bosons limits the range to extremely short distances before the EM interaction is stronger. The strength of gravity is $\sim 10^{-39}$ hence it is neglected. [1]

Interaction	Particle	Charge / e	Mass / GeV	Strength (α)
Strong	Gluon g	0	0	~ 1
Weak (Charged Current)	W^+	1	80.4	
	W^-	-1	80.4	10^{-6}
Weak (Neutral Current)	Z	0	91.2	
Electromagnetic (EM)	Photon γ	0	0	$\frac{1}{137}$

1.1.2.1 Quantum Chromodynamics

Quantum Chromodynamics (QCD) is the theory of the strong interaction, mediated by the gluon which couples to colour charge. It corresponds to the $SU(3)_c$ symmetry group of the overall SM. The strong interaction conserves energy, momentum, angular momentum and colour charge. Only quarks and gluons themselves possess colour charge, so while quarks are the only fermion to feel the strong interaction, gluons can self-couple. This self-coupling of gluons is the reason quarks are always observed in bound states.

1.1.2.2 Electroweak Unification

Electroweak Unification (EW) is the expression of the electromagnetic interaction described by Quantum Electrodynamics (QED) and the weak interaction as separate manifestations of a combined electroweak force in the Glashow-Weinberg-Salam model [5–7], which corresponds to the $SU(2)_L \times U(1)_\gamma$ symmetry group. QED describes the macroscopically observable $U(1)$ electromagnetic force with the photon as the mediating boson, and any interactions conserves energy, momentum, parity and charge and additionally never changes particle type through the interaction. The $SU(2)$ weak interaction is mediated by the charged current vector bosons W^+, W^- and the neutral current vector boson Z, which have large masses that limit the weak interaction to very short distances. The charged current interaction is capable of changing the flavour of a particle and also of violating parity in an interaction.

The weak interaction by itself was observed to diverge from observation at high energies, leading to the introduction of the unified theory. The combined $SU(2)_L \times U(1)_\gamma$ group produces four gauge bosons which mix to produce the more recognisable γ, W^+, W^- and Z bosons. The unified force couples to weak isospin, which allows self-coupling between the massive vector bosons, but not the photon as it does not carry electric charge.

While the weak interaction acts on both quarks and leptons, the quark sector is affected by the distinction between the mass eigenstates of quarks; the physically observed flavour sets, and the quark eigenstates of the weak interactions which are superpositions of the mass eigenstates. The effect of this quark mixing in the weak interaction is that different flavour changing interactions have different strengths. The mixing of the mass eigenstates (q) into weak eigenstates (q') is described by the Cabbibo-Kobayashi-Makasawa matrix [8, 9]:

$$\begin{pmatrix} d' \\ s' \\ b' \end{pmatrix} = \begin{pmatrix} V_{ud} & V_{us} & V_{ub} \\ V_{cd} & V_{cs} & V_{cb} \\ V_{td} & V_{ts} & V_{tb} \end{pmatrix} \begin{pmatrix} d \\ s \\ b \end{pmatrix} \tag{1.1}$$

1.1.3 Spontaneous Symmetry Breaking: The Higgs Boson

The gauge field theories used for the QCD and EW models when unaltered require massless gauge bosons in order to preserve gauge invariance, which follows from the Klein-Gordon equation:

$$\frac{\partial^2 \psi}{\partial t^2} = (\nabla^2 - m^2)\psi \tag{1.2}$$

This is satisfactory for the gluon and photon, but a separate theory is required to provide the mass for the $W^{\pm}$ and Z bosons. The Higgs Mechanism proposed introducing a scalar field that interacts with the $W^{\pm}$ and Z fields. In the Lagrangian formulation this results in a term akin to a mass term ($\propto \psi^2$) which effectively links that mass of the bosons to their coupling with this scalar field. This addition to the Lagrangian is still required to preserve the symmetry of the system and respect the gauge invariance, but is also required to have a non-zero expectation value for the field in the vacuum or ground state of space. The Higgs mechanism introduces the scalar field ϕ which has a potential energy $V(\phi)$:

To do: which spacing is prefeable

To do: cite

$$V(\phi) = a\phi^4 - b\phi^2 \tag{1.3}$$

This results in an equilibrium point ($\phi = 0$) that respects the symmetry, but is inherently unstable, with an infinite set of degenerate non-zero minima at $|\phi^2| = \frac{b}{2a}$ where the symmetry is *spontaneously* broken. This field in an analogous fashion to the other quantum fields of the SM can produce particles from excitations which form the physical Higgs Scalar Boson H. Confirmation of the Higgs boson as part of the SM was only achieved relatively recently [10, 11], where a a spin-0 boson consistent with the SM Higgs was observed. Subsequent measurements made have provided agreement on the new particle as the Higgs boson with a mass of 125.09 GeV [1]. Section 1.4 covers in more detail the production and behaviour of the Higgs boson in collider experiments.

1.2 Physics of *pp* Collisions

Experimental efforts to probe the Standard Model in recent times have focused on high-energy collider experiments, where beams of particle with equal energy are collided head on within detectors. For proton-proton (pp) collisions, matters are complicated as the colliding protons are composite particles, which at high energy consist of the three *valence* quarks *uud* and a sea of virtual quarks and gluons. Collectively these constituents are referred to as *partons* where each parton carries a fraction of the overall hadron momentum, and the interaction in the pp collision consists of elastic scattering between these partons. At a given energy scale Q^2 the probability that a parton i carries a fraction x_i of the overall momentum is described by the *parton distribution function* (PDF) $f_i(x, Q^2)$. These PDFs cannot be calculated from QCD but can be determined from experimental measurements, and collections of PDFs have been assembled from the leading collider experiments [12].

To do: decide if i want this italicising

In any particle interaction, the probability a particular reaction occurs is in proportion to the cross section of the reaction. The cross section for a short range, hard parton-parton collision is given by $\hat{\sigma}(Q^2)$, where scattering energy scale $Q^2 = x_1 x_2 E_{cm}^2$ in the parton-parton centre-of-mass frame where E_{cm} is the energy in the centre-of-mass frame. To compute the cross section σ for some hard process $pp \to X$, all possible combinations of incoming partons must be summed over and the momentum fractions integrated over while accounting for the PDFs:

$$\sigma = \sum_{i,j=q,g} \int dx_1 dx_2 f_i(x_1, Q^2) f_j(x_2, Q^2) \hat{\sigma}(Q^2) \tag{1.4}$$

To do: Think I need more here

1.2.1 Geometry?

To do: Necessary section?, good title?

The high energy protons used in collisions are automatically relativistic in nature, and as the momenta of the colliding partons are not guaranteed to be equal and opposing there is always an unknown element of longitudinal boosting in pp collisions. As a consequence, use of light-cone coordinates and some definitions of convenient quanties can be of benefit to pp collision analyses [13].

Typically the momentum in the transverse plane p_{T} is used for a particle, and the rapidity y of a particle with non-zero p_{T} is defined:

$$y = \frac{1}{2} \ln \frac{E + p_z}{E - p_z} \tag{1.5}$$

This rapidity y transforms additively to boosts along the z axis, so any rapidity difference between two objects is invariant to such boosts. For cases where the mass of a particle is negligible (highly relativistic particles) the rapidity can be related to the polar angle of the particle as the pseudo-rapidity η:

$$\eta = -\ln\tan\frac{\theta}{2} \tag{1.6}$$

1.3 Theoretical Predictions

To do: Not sure if this is a good title, or if aspects and commetary on the jet reconstrucion should go here too.

1.3.1 Monte-Carlo Event Generators

Use of Monte-Carlo event generators is critical to current high energy physics, where simulations of particle collisions are used to predict and prepare for real data-taking experiments, to obtain datasets of particular particle interactions and to train and optimise the tools used in analyses. Event generation for pp collisions is broken up into a few main steps to reduce the complexity of generating events with $O(1000)$ final state particles [14]:

- Hard process: a particular hard scatter event, the heart of the desired process, is simulated using the PDFS of the incoming components and perturbation theory to the desired accuracy (LO, NLO,. etc.) to evaluate the outgoing partons.
- Parton shower: The outgoing shower of partons is evaluated as a step-by-step simulation in momentum scales using QED and QCD, particularly the recursive radiation of gluons, developing an extended shower filled with mostly soft gluons up to a point where perturbation theory is no longer applicable.
- Hadronization: As perurbation theory breaks down, models that account for the confinement of partons into hadrons and converts the coloured partons of the shower step into colourless hadrons.
- Underlying event: Accounts for secondary parton interactions between remnants of the proton from the initial hard scatter to produce soft hadrons that overlap with the simulation of the hard process.
- Unstable particle decays: Account for the fact produced hadrons may be resonances not stable particles which go on to decay.

To do: Is a list suitable here?

Most leading generators like Pythia or Herwig make use of this chain of generation, and modern analyses will make use of multiple generators interfaced together to compute different steps with additional accuracy.

1.4 The Higgs Boson

Detecting the Standard Model Higgs boson is strongly dependent of the predominant production and decay channels for the Higgs boson, which in turn depend on the specifications(?) of the collider used for the search. In this section the relevant production and decay channels at the Large Hadron Collider (LHC) will be discussed.

1.4.1 Higgs Production

While there are many various methods for production of a Higgs boson, at the LHC the cross section is dominated by gloun-gloun fusion (ggF) as shown in figure 1.1, with the second largest cross-section arising from vector boson fusion (VBF). Other significant production processes are the WH/ZH or Higgs-strahlung production modes and associated production with top quarks (ttH) [15].

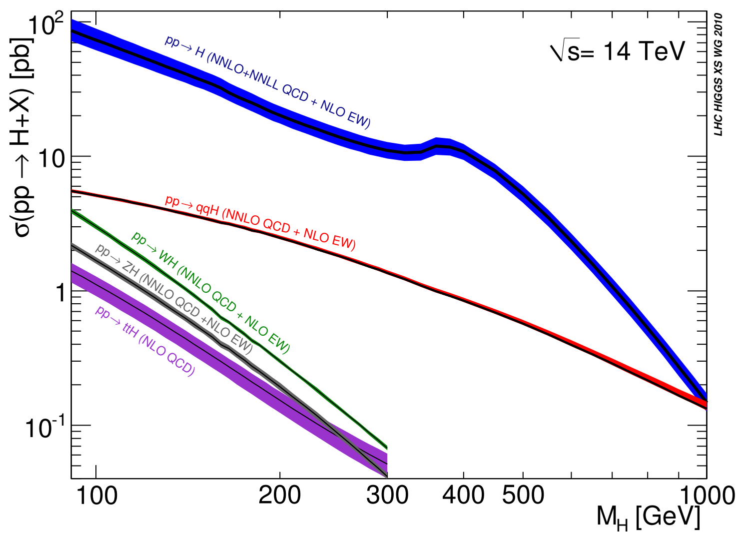

Figure 1.1: SM Higgs Production cross section for $\sqrt{s}$ = 14 TeV. $pp \to H$ corresponds to ggF production and $pp \to qqH$ VBF. [15]

1.4.1.1 Gluon-gluon fusion

5555

The dominant production mechanism for the Higgs boson in hadron colliders is the $gg \to H$ production via in intermediate quark loop. The dynamics of this mechanism are controlled by strong interactions, thus calculations of QCD corrections are necessary for any accurate predictions, and have been computed up from next-to-leading order (NLO) to N^{3}LO for the ggF process in recent years, along with the inclusion of Electro-Weak corrections in the cross section calculations [15].

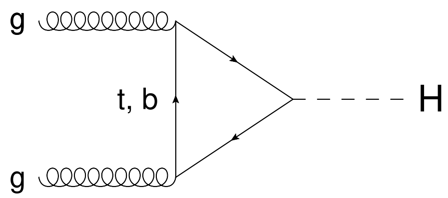

Figure 1.2: Lowest order Feynmann diagram contributing to $gg \to H$.

1.4.1.2 Vector Boson Fusion

Production of a Higgs boson from the fusion of vector bosons radiated from initial-state quarks is the second largest cross-section at the LHC, as is useful as a production mode due to topological characteristics which can distinguish the event from ggF. In VBF, the Higgs boson is produced along with two jets in the forward regions of the detector , which originate from the initial quarks as shown in Figure 1.3. In addition central jet activity is suppressed due to the lack of colour exchange between quarks [16]. These distinct features mean that while the cross section for VBF at a Higgs mass of < 200 GeV is dominated by ggF, the easy to detect signature means the channel is a cornerstone of searches for the Higgs boson.

Maybe need to link to the detector section

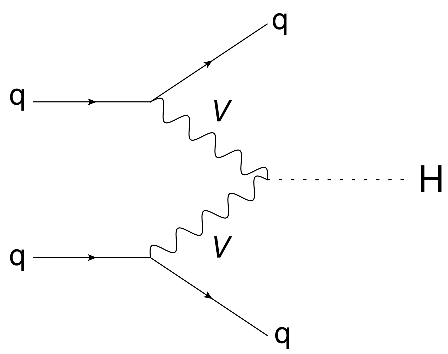

Figure 1.3: Feynmann diagram for the production of a Higgs boson via vector boson (V) fusion, where q denotes any quark or antiquark

1.4.2 Higgs Decay

The branching ratios for decays of the Higgs boson in the Standard Model have been extensively determined using Monte-Carlo event generators. As is to be expected, the relative cross-sections of the decay modes are strongly dependent on the mass of the Higgs boson, as highlighted in Figure 1.4.

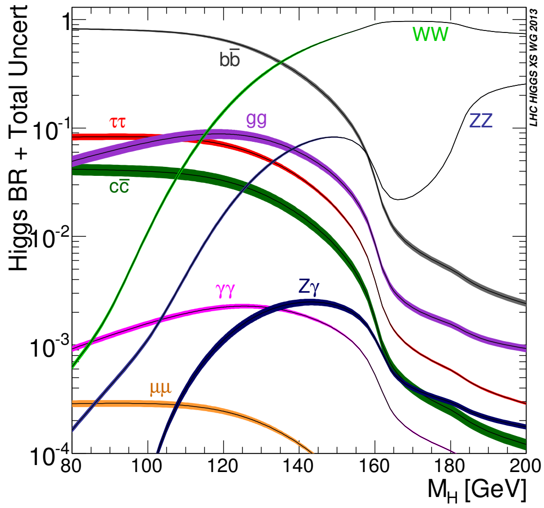

Figure 1.4: Higgs decay branching ratios for the low mass region with their uncertainties [17].

While observations consistent with the Standard Model Higgs boson have been made for the $H \to \gamma\gamma$, $H \to ZZ$, $H \to W^+W^-$ and $H \to \tau^+\tau^-$ channels, observation of th $H \to bb$ decay channel is significantly hindered owing to the large background from multijet production (Section **??** maybe?) in hadron collisions. Despite this, the topology of the VBF production mechanism makes it a viable option for observation of the $b\bar{b}$ decay channel.

1.4.3 Vector Boson Fusion

CHAPTER 2

DETECTOR

2.1 The Large Hadron Collider

The Large Hadron Collider (LHC) is a circular particle accelerator operated at European Organisation for Nuclear Research (CERN, Conseil Européen pour la Recherche nucleéaire). Currently the largest accelerator in the world, the LHC is designed to collide heavy ions or opposing proton beams for a peak design centre-of-mass energy $\sqrt{s} = 14$TeV with a luminosity of 10^{34}cm^{-2}s^{-1} [18]. The forst proton beams were circulated in the LHC in 2008, with Run 1 of LHC data taking being conducted until 2013, at which point the machine was shut down for maintenance. Following on from the initial operations, Run-2 of the LHC has been undergoing since 2015, operating at $\sqrt{s} = 13$TeV.

To do: need to explain the concept of luminosity somewhere?

The principle LHC ring consists of eight pairs of alternating long arc sections and short straight insertion sections, situated within the underground tunnel excavated for the older Large Electron Positron Collider experiment [19, 20]. The arc sections contain the dipole magnets used to bend the particle beam around the ring, while the straight sections contain four interaction points, at each of which the large experiments are located. The remaining straight sections contain the operational systems of the LHC: beam acceleration, injection, dumping and collimation. The proton beams are genereated outside the principle ring and inserted into the ring by the LHC injector chain, a syequence of smaller accelerators which are used to bring the proton beams up to a suitable energy for injection. The proton beams are arranged such that the protons move in bunches of $O(10^{11})$ protons, with multiple byunches placed into trains. Once a beam is accelerated to the target energy interactions begin, at which point a steady stream of interactions is produced until the beam is replaced due to general decay of the interaction fate or beam instabilities.

The large experiments at the LHC are ATLAS (A Toroidal LHC ApparatuS), CMS (Compact Muon Solenoid), LHCb (LHC beauty) and ALICE (A Large Ion Collider Experiment). LHCb is a forward spectrometer heavy flavour experiment, designed to study flavour physics with emphasis on the b quark and on matter/anti-matter asymmetry. ALICE focuses on the collisions of heavy ions, while ATLAS and CMS are general purpose detectors to conduct experiments across a broad range of modern physics research areas.

2.1.1 Run Conditions in 2016

Over the course of 2016 the LHC beam was operated predominantly with two beams of energy 6.5TeV for $\sqrt{s}$ = 13TeV following beam commissioning runs. Over the course of the 2016 data-taking the ATLAS and CMS experiments achieved an integrated luminosity of 40 fb^{-1} with a peak instantaneous luminosity of 1.4×10^{34}cm^{-2}s^{-1} with 2220 bunches per beam [21].

To do: Definitely think something to do with lumi might be needed somewhere, and on byunchspacings

2.2 The ATLAS Detector

To do: Detail level?

The ATLAS detector [22] is a multi-detector designed to manage with the experimental conditions of the LHC and study a broad selection of physics phenomena. The detector is cylindrical in structure with the axis alignewd to the beam path and nominally forward-backward symmetric in terms of the beam collision point at the centre of the detector. The detector provides approximately 4π solid angle coverage around the interaction point to detect as many collision products as possible.

The structure of the ATLAS detector is composed of concentric subsystems around the interaction point. The Inner Detector is the component closest to the interaction point, and is contained in a superconducting solenoid. This is surrounded by high-granularity calorimeters and an extensive muon spectrometer contained within and eight-fold azimuthally symmetric arrangement of three large toroidal magnets. A schematic representation of the ATLAS detector is shown in Figure 2.1. The subsystems are arranged into three cryostats, two *endcaps* located on the ends of the detector and the central *barrel* section. Discussion of the coordinates and quantities used in the detector is found in Section 1.2.1. A summary of the operational paramaters of the principle detector components is given in Table **??**.

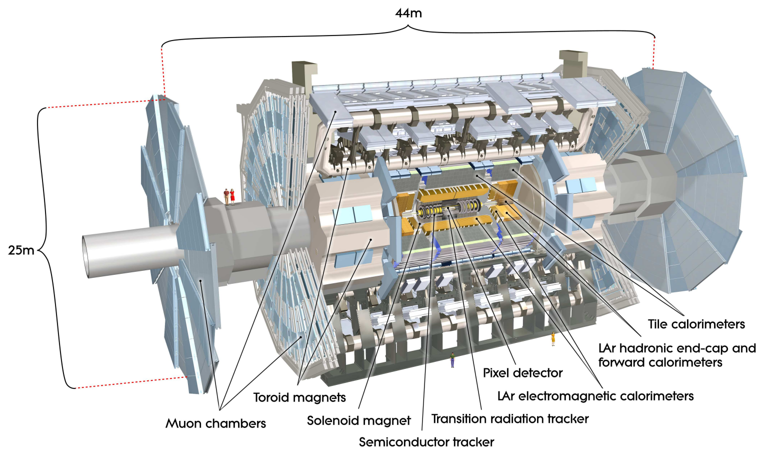

Figure 2.1: Schematic cut-away of the ATLAS detector [23].

2.2.1 Inner Detector

The Inner Detector (ID) provides pattern recognition, momentum measurements, electron identification and measurements of both primary and secondary vertices to efficiently identify jets containing b-hadron within a pseudorapidity range $|\eta| < 2.5$. The ID itself is contained within a 2 T solenoidal field, and makes use of a combination of slilicon pixel and strip detectors at the core of the tracking volume wrapped with straw-tube tracking detectors in the Transition Radiation Tracker to perform particle identification and tracking.

2.2.2 Calorimeters

Calorimeters are used to measure the energy of any particle incident into the calorimeter. Incident particles cause the development of either Electromagnetic (EM) or hadronic showers within the calorimeter substrate, and the energy deposited in this shower can be used to calculate the incident energy. The ATLAS calorimetry system consists of a combination of EM and hadronic calorimeters arranged with full ϕ-symmetry around the beam axis. The combination of all separate calorimeters provides pseudorapidity coverage in the range $|\eta| < 4.9$. Within the pseudorapidity region of the inner detector, the fine granularity of EM calorimeters is optimised for measurements of electron and photon tracks and momenta, while the coarser hadronic calorimeters contained in the remainder of the calorimeter system are sufficient for jet reconstruction and missing energy calculations. The structure and design of the calorimeter components has been optimised to provide complete azimuthal coverage, take into account the engineering requirements for assembling the detector for desired calorimitry performance and account for radiation considerations between the different detector components [22].

The EM calorimeter is a lead-Liquid-Argon (LAr) detector, which is split into a barrel section (EMB, $|\eta| < 1.475$) and two endcap sections (EMEC, $1.375 < |\eta| < 3.2$) with each section contained in a separate cryostat. The EMB consists of two identical half-barrels split by a small gap at $z = 0$. Each of the EMEC sections is a pair of coaxial wheels, with the inner and outer sections covering regions $1.375 < |\eta| < 2.5$ and $2.5 < |\eta| < 3.2$ respectively.

Hadronic calorimetry for particles undergoing the strong interaction is provided by the steel/scintillator tile calorimeter for pseudorapidity values of $|\eta| < 1.7$, and by the LAr flat-plate Hadronic Endcap Calorimeter (HEC) for $1.5 < |\eta| < 3.2$. The tile calorimter directly surrounds teh EM calorimeter, and is split into a central barrel section for $|\eta| < 1.0$ and two extended barrel sections covering $0.8 < |\eta| < 1.7$. The HEC akin to the EMEC consists of two separate wheels per end-cap covering $1.5 < |\eta| < 3.2$, and is contained within the same cryostat as the EMEC. The detector consists of alternating copper plates with LAr gaps to act as the active medium.

In addition to the barrel and end-cap calorimeters, the LAr Forward Calorimeter is contained within the end-cap cryostat (The FCal is omitted from Figure 2.1) and is designed to perform both EM and hadronic calorimetry across a pseudorapidity range of $3.1 < |\eta| < 4.9$ using a combination of copper/LAr (EM) and tungsten/LAr (hadronic) calorimeter components.

2.2.3 Muon Spectrometer

The muon spectrometer is the outermost component of the ATLAS detector, measuring trajectory and momentum of muons from the interactions within a pseudorapidity range of $|\eta| < 2.7$. The muon system consists of three large superconducting coils that deflect the muon trajectories. The system is designed for high precision tracking of the minimally ionising muons and for use in the triggering system.

Table 2.1: Performance goals and operational ranges for principle components of the ATLAS detector. [22]

System	Component	η Coverage	Resolution
Tracking		$0 < \|\eta\| < 2.5$	$\sigma_{p_T}/\mathrm{p_T} = 0.05\%\ p_T \oplus 1\%$
EM Calorimetry	EMB	$0 < \|\eta\| < 1.475$	$\sigma_E/E = 10\%/\sqrt{E} \oplus 0.7\%$
	EMEC (Inner)	$1.375 < \|\eta\| < 2.5$	
	EMEC (Outer)	$2.5 < \|\eta\| < 3.2$	
Hadronic Calorimetry	Tile (Barrel)	$0 < \|\eta\| < 1$	$\sigma_E/E = 50\%/\sqrt{E} \oplus 3\%$
	Tile (Extended)	$0.8 < \|\eta\| < 1.7$	
	HEC	$1.5 < \|\eta\| < 3.2$	
Forward Calorimetry	FCal	$3.1 < \|\eta\| < 4.9$	$\sigma_E/E = 100\%/\sqrt{E} \oplus 10\%$
Muon Spectrometer		$0 < \|\eta\| < 2.7$	$\sigma_{p_T}/\mathrm{p_T} = 10\%$ at$p_T = 1TeV$

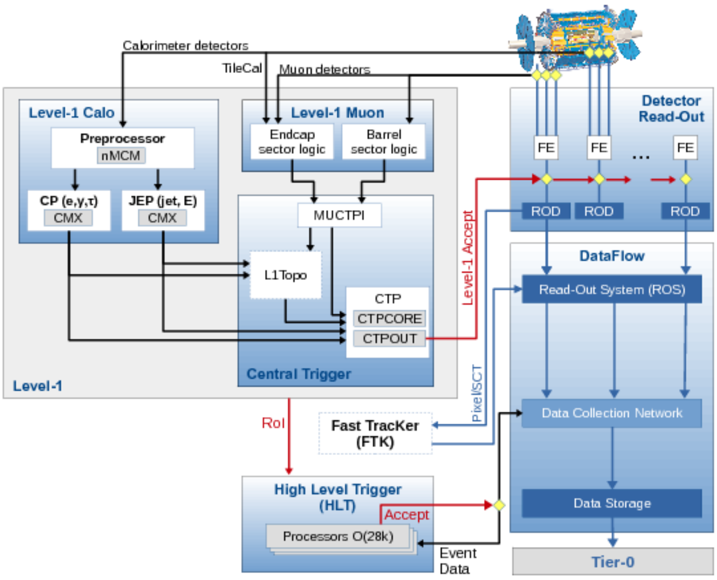

Figure 2.2: Schematic plot of the ATLAS Trigger and Data acquisition system [24].

2.3 Triggers

When operating at the design luminosity, the LHC produces a bunch-crossing rate of 40 MHz [**?**]. This extreme rate of interaction necessitates a trigger system to reduce the output rate to a suitable level for offline processing, which is predominantly limited by the rate at which data can be written to disk. The limit of the output rate is determined by the computational capabilities, specifically the average data rate of output. The trigger system selects events by quickly identifying distinguishing features of events (i.e. signatures of muons, electrons, jet and *b*-jet objects) and using combinations of these signatures to signify an event as relevant for further analysis. Overall usage of the trigger system brings the output rate down to 1 kHz with a maximum L1 rate of 100 kHz.

The ATLAS trigger system consists of a chain of selection stages of increasing severity and corresponding decrease in rate. A schematic outline of the trigger system is shown in Figure **??**. This outline covers both the logical process and the transfer of data between components of the trigger chain. The principle decision logic of the trigger system is however contained in two sections, the L1 trigger sytem and the High Level Trigger (HLT).

To do: THis is not a suitable plot

The L1 trigger system [25] is a hardware based decision system, using fast custom electronics to minimise latency in any decision. The L! uses reduced-granularity data from the calorimetric and muon detectors, reconstructed objects and missing and total transverse energy. The high bunch-crossing rate means instantaneous processing of the event is non-viable, so event readouts word choice are stored in a buffer chain of events to be evaluated with a fixed permitted decision time per event. Along with this first selection, the L1 trigger defines *Regions of Interest* (RoIs) in the phase space within the detector, which are labelled for investigation in the HLT. TALK ABOUT RATE

In contrast to the hardware computation of the L1 system, the HLT consists of software algorithms running in a farm of $\approx$ 40000 interconnected processors [**?**]. Following acceptance of an event by the L1 trigger, events are transferred from the initial data pipeline to dedecated readout buffers for the HLT. The HLT performs processing on the events using finer-granularity information from teh calorimeters and muon spectrometer, along with making use of information from the ID, which is unavailable to L1. This more precise data is the computed using object reconstruction algorithms similar to the offline reconstruction. A decision at HLT level is managed by a trigger chain, which is a sequence of specific criteria and algorithms evaluated on an event in sequence. The HLT provides $O(1000)$ independent trigger chains for evalutating events. Along with the partial reconstruction of relevant objects, the HLT is capable of performing complete reconstruction of an event, and also capable of writing out these partial or complete reconstructions of an event into different data streams from the complete detector readout for use in analysis.

2.4 Object Reconstruction

2.4.1 Jets

2.4.2 *b*-jets

2.5 *b*-Tagging

Identification of b-quark jets in ATLAS is based on combining the output of three separate b-tagging algorithms: Impact Parameter based (IP2D and IP3D, described in Section 2.5.0.1), Secondary Vertex based (SV, described in Section 2.5.0.2) and Decay Chain based (JetFitter, described in Section 2.5.0.3)into a multivariate discriminant (MV2, covered in Section 2.5.1) which is used to distinguish the jet flavours. These algorithms have undergone continuous improvement over the Run-2 cycle of the LHC to improve the separation of jet flavours.

2.5.0.1 IP2D and IP3D: Impact Parameter based Algorithms

The typical topology for a b-hadron of a secondary vertex displaced from the hard scatter interaction point as a results of the lifetime of b-quark is used as the basis of these algorithms. Impact parameters of tracks from the secondary vertex are computed with respect to the primary vertex of the interaction. The IP2D algorithm uses a transverse impact parameter (d_0) defined as the distance of closest approach of a track to the primary vertex in r-ϕ plane around the vertex. The IP3D algorithm uses both the transverse and a correlated longitudinal impact parameter ($z_0 \sin\theta$), defined as the distance between the point of closest approach in r-ϕ and the primary vertex in the longitudinal plane. . These parameters typically have large values as a result of the lifetime of b-quark . The signs of the impact parameters are also defined to take account of if they lie infront or behind the primary vertex with respect to the jet direction, with secondary vertices occuring behind the primary vertex normally due to background.

To do: I kind of want a diagram here, but that doesn't appear to be the norm

The significance of the impact parameter values ($\frac{d_0}{\sigma_{d_0}}$, $\frac{z_0}{\sigma_{z_0 \sin\theta}}$) for each track are compared to probability density functions obtained from reference histograms derived from Monte Carlo simulation, with each track being compared to a selection of reference track categories. This results in weights which are combined using a log-likelihood ratio (LLR) discriminant to compute an overall jet weight separating the b, c, and light-jet flavours from each other. [26, 27]

2.5.0.2 SV1: Secondary Vertex Finding algorithm

The secondary vertex algorithm uses the decay products of the b-hadron to reconstruct a distinct secondary vertex. The algorithm uses all tracks that are significantly displaced from the primary vertex associated with the jet, forming vertex candidates for all pairs of track, while rejecting any vertices that would be associated with decay of long lived particles (e.g. K_s, Λ), photon conversions or interactions with the material in the detector. The tracks forming these vertex candidates are then iteratively combined and refined to remove outliers beyond a χ^2 threshold leaving a single inclusive vertex.

The properties of this secondary vertex are used to differentiate the flavour of the jet. The SV1 algorithm is based on a LLR formalism similar to the IP algorithms, and makes use ot the invariant mass of all charged tracks used to reconstruct the vertex, the number of two track vertices and the ratio of the invariant mass of the charged tracks to the invariant mass off all tracks. In addition the algorithm is signed in a similar fashion to the IP algorithms and uses the ΔR between the jet direction and secondary vertex displacement direction in the LLR calculation. The algorithm uses distributions of these variables to distinguish be tween the jet flavours. [26, 27]

Might be worth mentioning the way these are trained

2.5.0.3 JetFitter: Decay Chain Multi based Algorithm

The JetFitter algorithm exploits the topological structure of weak b-hadron and c-hadron decays inside the jet to reconstruct a full b-hadron decay chain. A Kalman filter is used to find a common line between the on which lie the b, c and primary vertices to approximate the b-hadron

To do: Either understand or just cite flight path. A selection of variables relating to the primary vertex and the properties of the tracks associated with the jet are used as input nodes in a neural network. This neural network uses the input variables and p_{T} and $|\eta|$ variables from the jets, reweighted in the kinematic variables to ensure the spectra of the kinematics are not used in the training of the neural net. The neural network outputs a discriminating variable relating to each jet flavour which are used to tag the jets. [**?**]

2.5.1 Multivariate Algorithm

The output variables of the three basic algorithms described prior are combined as input into the Multivariate Algorithm MV2. MV2 is a Boosted Decision Tree (BDT) algorithm which has been trained on $t\bar{t}$ events to discriminate b-jets from light and c-jets . The algorithm makes use of the jet kinematics in addition to the tagger input variables to prevent the kinematic spectra of the training sample from being used as discriminating factor. The MV2 algorithm is an revised version of the MV1 algorithm used during Run-1 of the LHC, and has three sub-variants (MV2c00, MV2c10, and MV2c20) of the algorithm distinguished by the exact background composition of the training sample. The naming convention initially referred to the c-jet composition of the training sample, e.g. for MV2c20 the b-jets are designated as signal jets where a mixture of 80% light jets and 2-% c-jets was designated as background.

Why?

list all input variables?

The MV2 algorithm has a set of working points, defined by a single value of the output distribution of the algorithm, which are configured to provide a specific b-jet selection efficiency on the training $t\bar{t}$ sample. Rather than being used independently, physics analyses will make use of several working points as an increase in b-jet efficiency (corresponding to *looser* b-jet selection) will bring an increased mistag rate of light and c-jets .

These algorithms were refined prior to the 2016 Run-2 data-taking session in response to c-jets limiting physics analyses more the light-jets. This change to enhance the c-jet rejection meant that for the MV2c10, the c-jet fraction was set to 7% in training and the fraction for MV2c20 was 15%. There were a selection of other improvements to the algorithm made to the algorithm relating to the BDT training parameters and the use of the basic algorithms before the 2016 data taking. With these refinements, the MV2c10 algorithm was found to provide a comparable level of light-jet rejection to the original 2015 Mv2c20 algorithm with impoved c-jet rejection, so was chosen as the standard algorithm for 2016 analyses. [26]

2.6 Trigger Level Analysis

CHAPTER 3

EVENT SELECTION

This section describes the selection criteria required for the events and reconstructed objects used in the analysis. These cuts and criteria are designed with the VBF $H \to b\bar{b}$ event topology in mind, along with the limitations introduced by considering the available trigger chains as discussed in Section **??**. These cuts are applied in the VBF $H \to b\bar{b}$ analysis and the direct object comparison covered in Chapter 4.

3.1 Events

Data events were required to pass the all year 25ns Good Runs List[a] **??** and also be Clean **??**.

3.2 Offline Jets

Offline jet reconstruction was performed by the anti-k_t algorithm (R=0.4) as discussed in Section **??**. Jets were calibrated in line with the 20.7 recommendations **??**. When considering individual jets during the analysis, all jets were required to have a $p_{\mathrm{T}} > 45$ GeV to be recorded.

3.3 Online Jets

Online Jet reconstruction is a mystery. A full collection of online jets was recovered by extracting the split jets (Section

[a] data16_13TeV.periodAllYear_DetStatus-v88-pro20-21_DQDefects-00-02-04_PHYS_StandardGRL_All_Good_25ns.xml

3.4 Offline *b*-jets

The specifics of *b*-tagging are covered in Section 2.5. Offline *b*-jets were tagged using the *MV2c10*-tagger[b] with two defined efficiency working points: *Tight*, with an overall efficiency of 70% and *Loose* with 85% tagging efficiency.

3.5 Online *b*-jets

Online *b*-jets were tagged using the *MV2c20*-tagger[c] with two defined efficiency working points: *Tight*, with an overall efficiency of 70% and *Loose* with 85% tagging efficiency.

[b] Jan 2017 Recommendations: 2016-20_7-13TeV-MC15-CDI-2017-01-31_v1.root
[c] Mar 2016 Recommendations: 2016-Winter-13TeV-MC15-CDI-March10_v1.root

CHAPTER 4

OBJECT PERFORMANCE

Prior to conducting a full study of TLA on the VBF $H \to b\bar{b}$ channel, the features of jet objects reconstructed offline and within the HLT were compared to identify any performance differences in the base components of an event reconstruction. The jet objects were compared on a one to one basis, by matching an online jet to an offline jet by requiring the ΔR value between the two jets to be below a threshold value of 0.3[a].

To do: Does this need a plot, or is this sufficient?

4.1 Leading *b*-jets

The leading p_{T} offline *b*-jet selected using the *Tight* working point was matched to a corresponding *b*-jet using ΔR matching. The following figures show the ratio of the difference in value between the offline and online jet calculated using the following formula for jet feature X:

$$\Delta X_{ratio} = \frac{X_{Offline} - X_{Online}}{X_{Offline}} \tag{4.1}$$

where $X_{Offline}$ is the value of the feature on the offline jet, and X_{Online} is from the HLT jet.

[a]Determined from a plot of ΔR values between all pairs of jets

4.1.1 Monte-Carlo

4.1.1.1 Plots of b-jet features

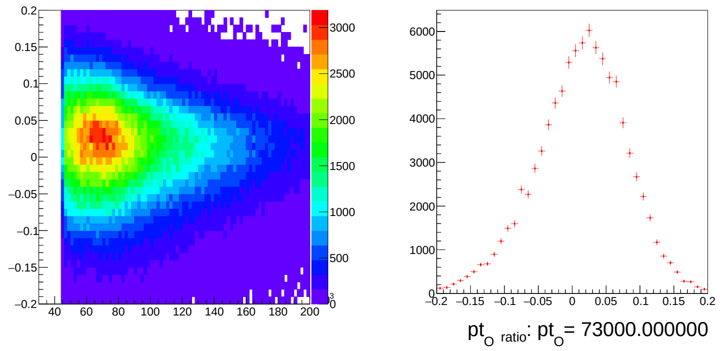

Figure 4.1: $\Delta p_{\mathrm{T}\ ratio}$ for the leading p_{T} b-jet from MC events against p_{T} of the offline b-jet. A slice across the y-axis has been taken at $p_{\mathrm{T}} = 79$GeV.

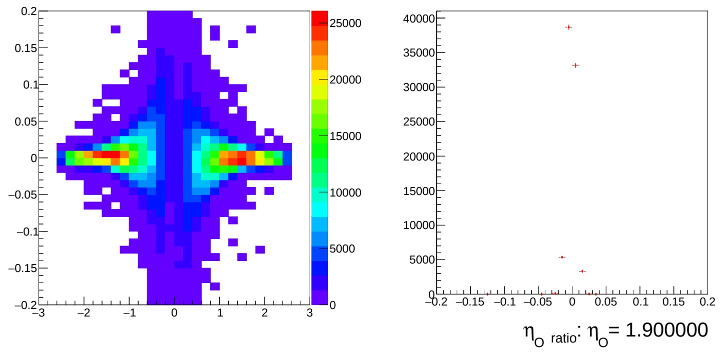

Figure 4.2: $\Delta\eta_{ratio}$ for the leading p_{T} b-jet from MC events against η of the offline b-jet. A slice across the y-axis has been taken at $\eta = -1.9$.

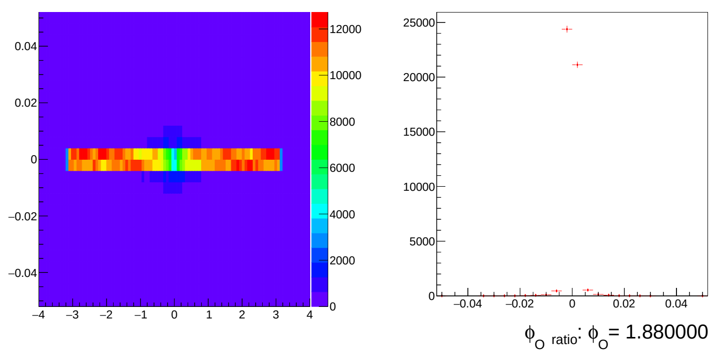

Figure 4.3: $\Delta\phi_{ratio}$ for the leading p_{T} b-jet from MC events against ϕ of the offline b-jet. A slice across the y-axis has been taken at $\phi = -1.64$.

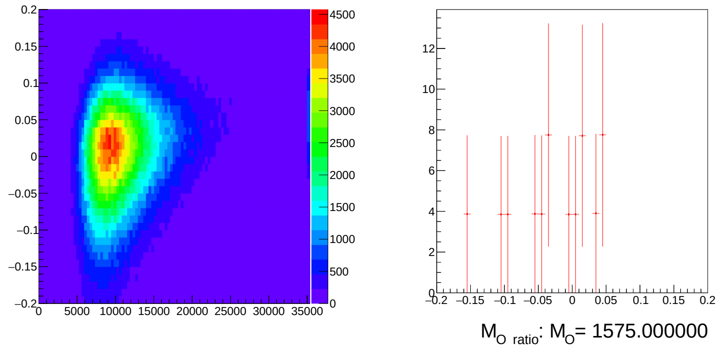

Figure 4.4: ΔM_{ratio} for the leading p_{T} b-jet from MC events against M of the offline b-jet. A slice across the y-axis has been taken at $M = 7$GeV.

4.1.1.2 Conclusions from MC jet features

4.1.2 Data

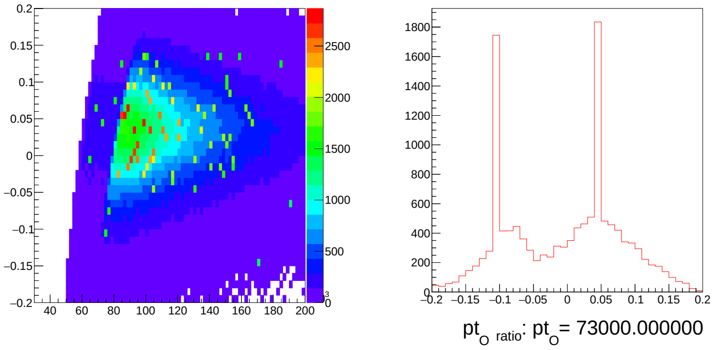

Figure 4.5: $\Delta p_{\mathrm{T}\ ratio}$ for the leading p_{T} b-jet from data events against p_{T} of the offline b-jet. A slice across the y-axis has been taken at $p_{\mathrm{T}} = 79$GeV.

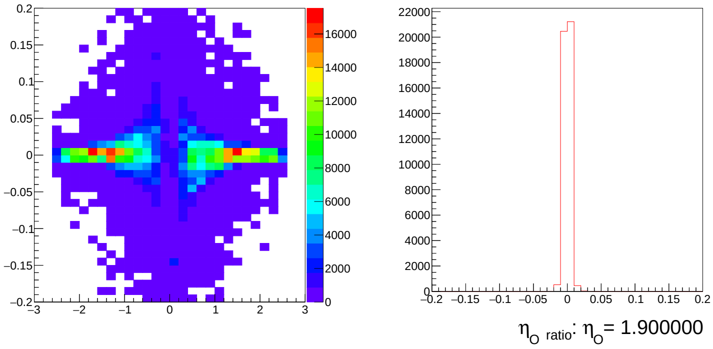

Figure 4.6: $\Delta\eta_{ratio}$ for the leading p_{T} b-jet from data events against η of the offline b-jet. A slice across the y-axis has been taken at $\eta = -1.9$.

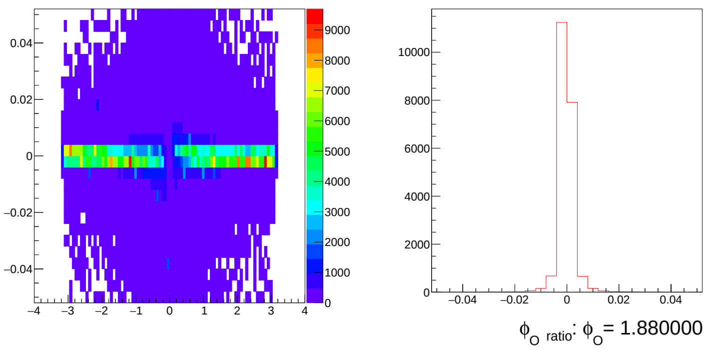

Figure 4.7: $\Delta\phi_{ratio}$ for the leading p_{T} b-jet from data events against ϕ of the offline b-jet. A slice across the y-axis has been taken at $\phi = -1.64$.

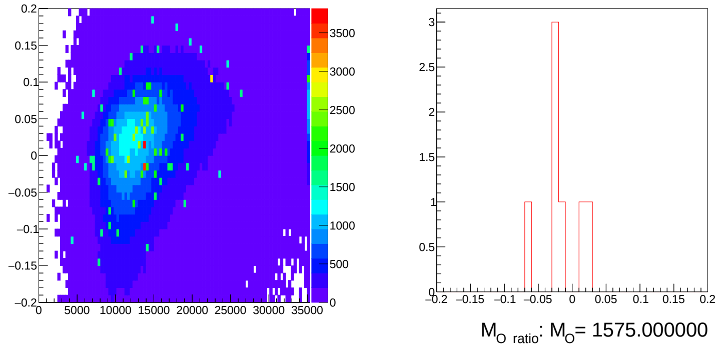

Figure 4.8: ΔM_{ratio} for the leading p_{T} b-jet from data events against M of the offline b-jet. A slice across the y-axis has been taken at $M = 7$GeV.

4.2 Leading Non *b*-jets

The non b-jet category is defined as the jets exclusive to those tagged in Section 4.1. Again, the leading p_{T} offline jet from this list is matched with an online jet for the comparison.

4.2.1 Monte-Carlo

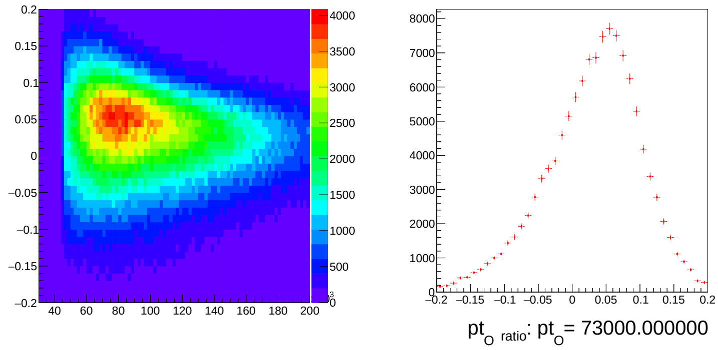

Figure 4.9: $\Delta p_{\mathrm{T}\ ratio}$ for the leading p_{T} non b-jet from MC events against p_{T} of the offline b-jet.

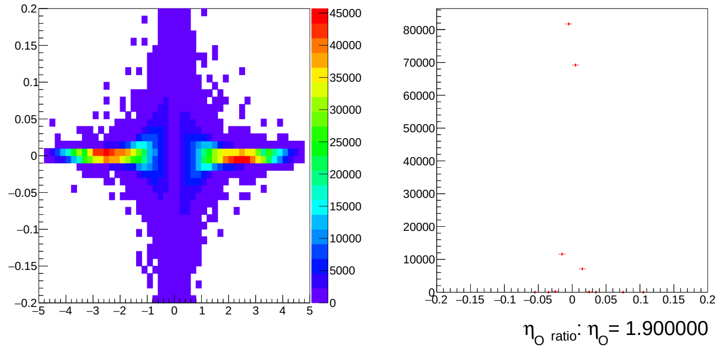

Figure 4.10: $\varDelta\eta_{ratio}$ for the leading p_{T} non b-jet from MC events against η of the offline b-jet.

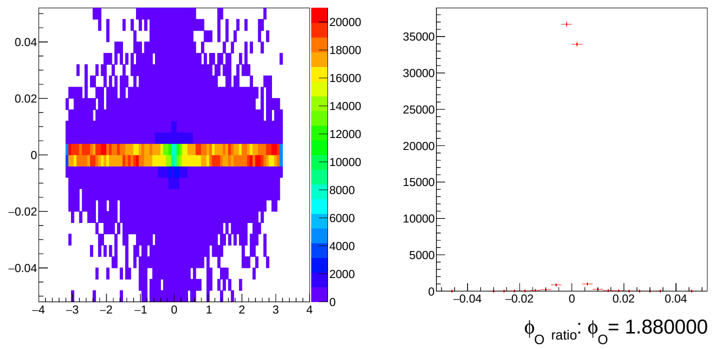

Figure 4.11: $\varDelta\phi_{ratio}$ for the leading p_{T} non b-jet from MC events against ϕ of the offline b-jet.

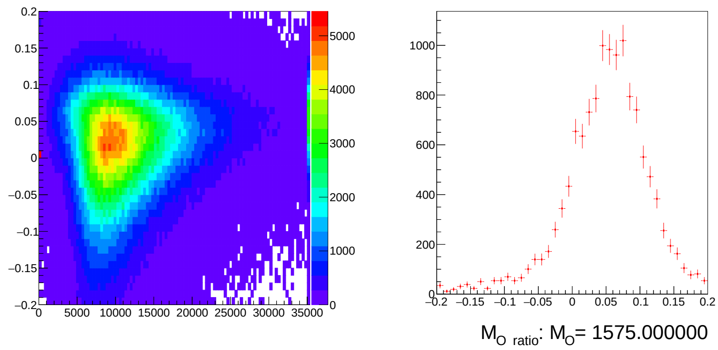

Figure 4.12: $\varDelta M_{ratio}$ for the leading p_{T} non b-jet from MC events against M of the offline b-jet.

4.2.2 Data

spacing

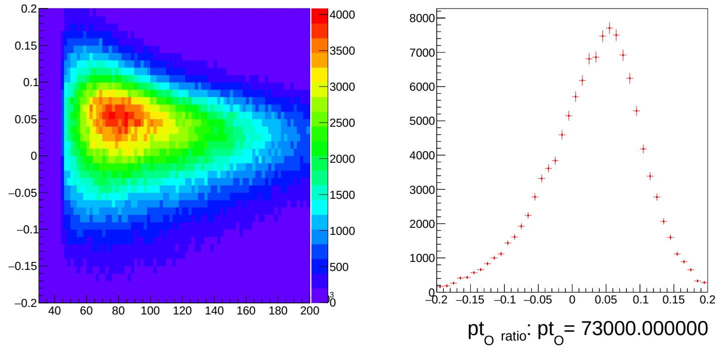

Figure 4.13: $\Delta p_{\mathrm{T}\ ratio}$ for the leading p_{T} non b-jet from Data events against p_{T} of the offline b-jet.

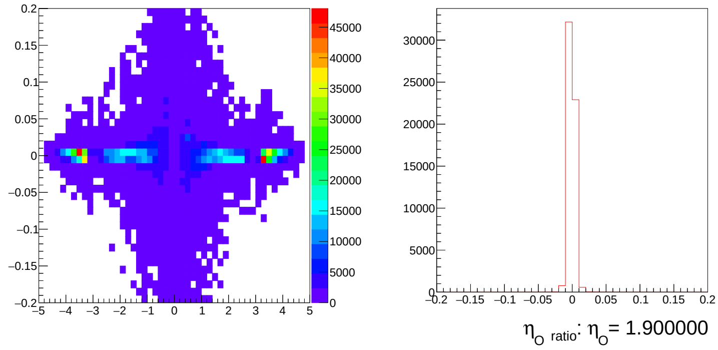

Figure 4.14: $\Delta\eta_{ratio}$ for the leading p_{T} non b-jet from Data events against η of the offline b-jet.

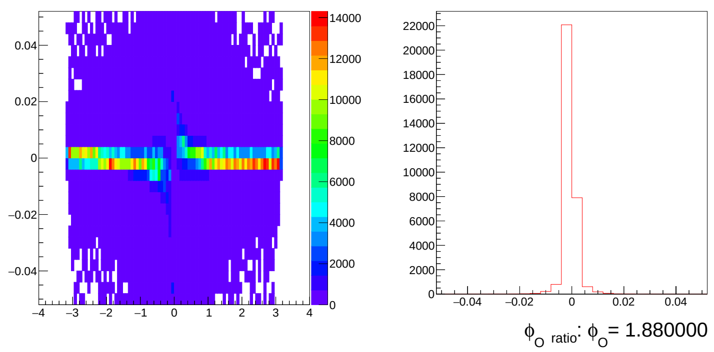

Figure 4.15: $\Delta\phi_{ratio}$ for the leading p_{T} non b-jet from Data events against ϕ of the offline b-jet.

4.3 Central Jets

4.3.1 Monte-Carlo

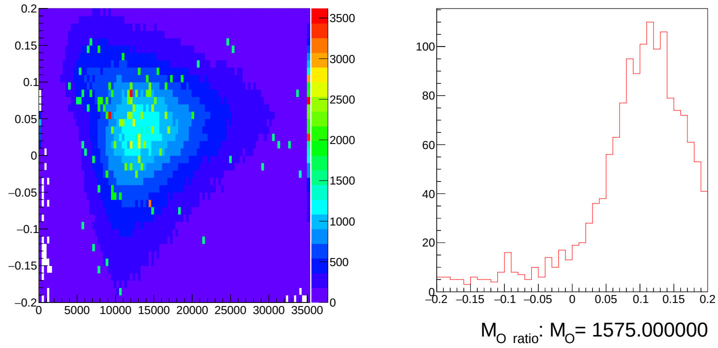

Figure 4.16: ΔM_{ratio} for the leading p_{T} non b-jet from Data events against M of the offline b-jet.

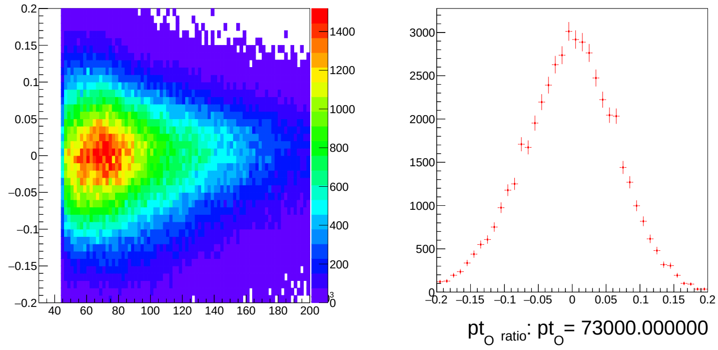

Figure 4.17: $\Delta p_{\mathrm{T}\ ratio}$ for the leading p_{T} b-jet with $0 < \eta < 1$ from MC events against p_{T} of the offline b-jet. A slice across the y-axis has been taken at $p_{\mathrm{T}} = 79$GeV.

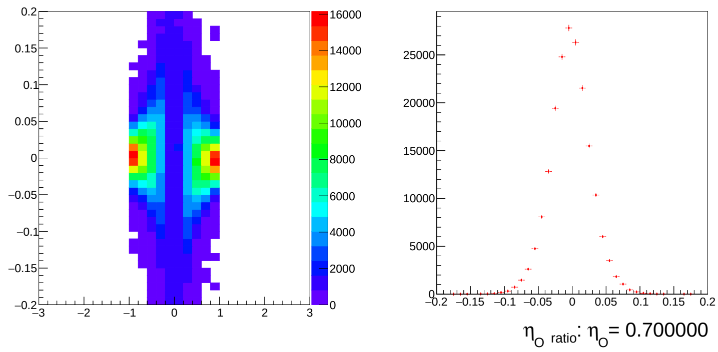

Figure 4.18: $\Delta\eta_{ratio}$ for the leading p_{T} b-jet with $0 < \eta < 1$ from MC events against η of the offline b-jet. A slice across the y-axis has been taken at $\eta = -1.9$.

4.3.2 Data

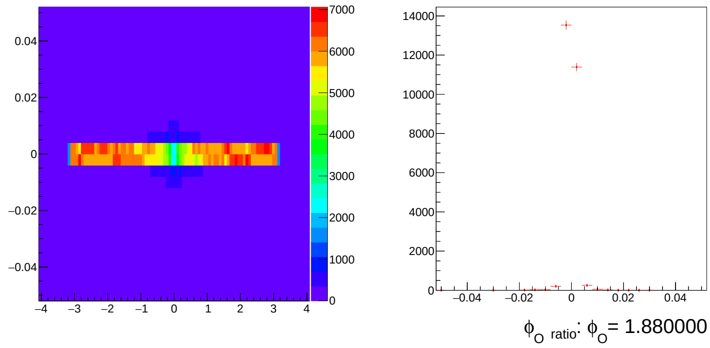

Figure 4.19: $\Delta\phi_{ratio}$ for the leading p_{T} b-jet with $0 < \eta < 1$ from MC events against ϕ of the offline b-jet. A slice across the y-axis has been taken at $\phi = -1.64$.

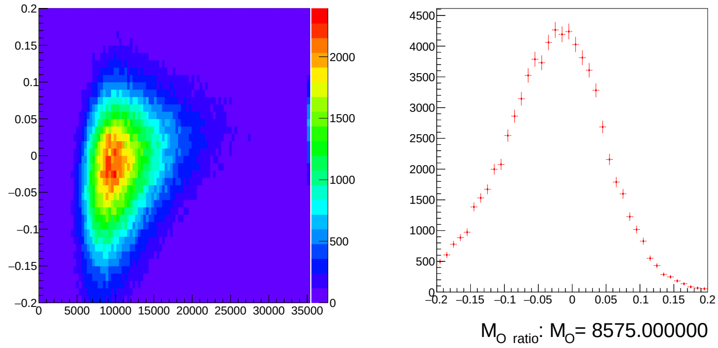

Figure 4.20: ΔM_{ratio} for the leading p_{T} b-jet with $0 < \eta < 1$ from MC events against M of the offline b-jet. A slice across the y-axis has been taken at $M = 7$GeV.

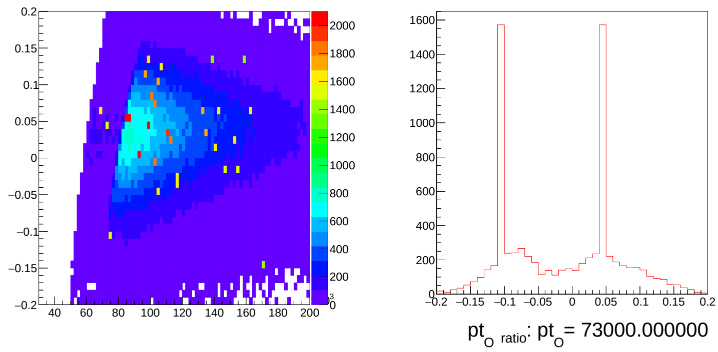

Figure 4.21: $\Delta p_{\mathrm{T}\ ratio}$ for the leading p_{T} b-jet with $0 < \eta < 1$ from Data events against p_{T} of the offline b-jet. A slice across the y-axis has been taken at $p_{\mathrm{T}} = 79$GeV.

4.3.3 Non b Jets

4.3.4 Monte-Carlo

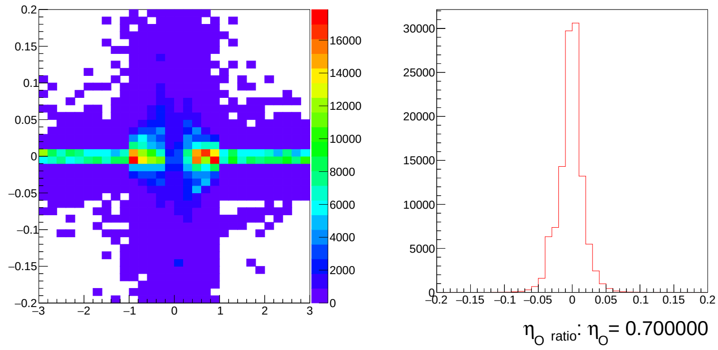

Figure 4.22: $\Delta\eta_{ratio}$ for the leading p_{T} b-jet with $0 < \eta < 1$ from Data events against η of the offline b-jet. A slice across the y-axis has been taken at $\eta = -1.9$.

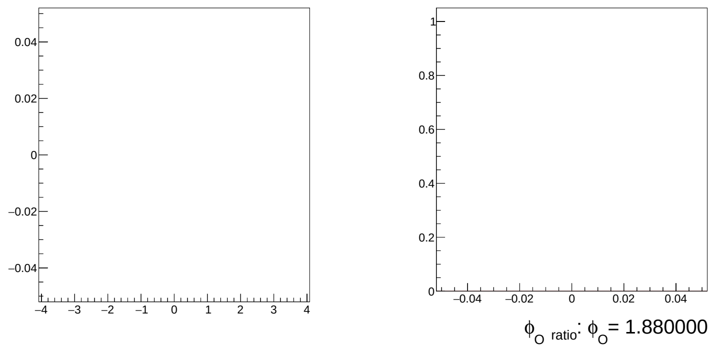

Figure 4.23: $\Delta\phi_{ratio}$ for the leading p_{T} b-jet with $0 < \eta < 1$ from Data events against ϕ of the offline b-jet. A slice across the y-axis has been taken at $\phi = -1.64$.

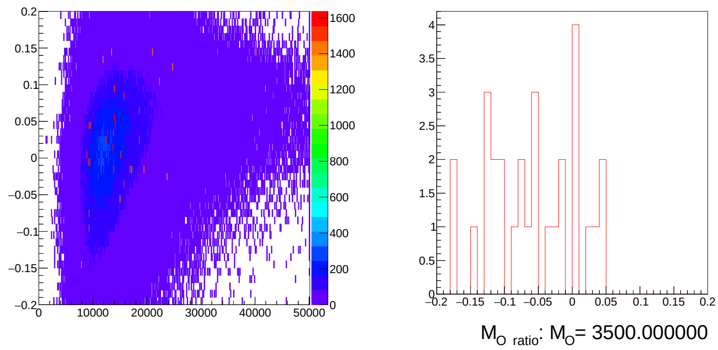

Figure 4.24: ΔM_{ratio} for the leading p_{T} b-jet with $0 < \eta < 1$ from Data events against M of the offline b-jet. A slice across the y-axis has been taken at $M = 7$GeV.

4.3.5 Data

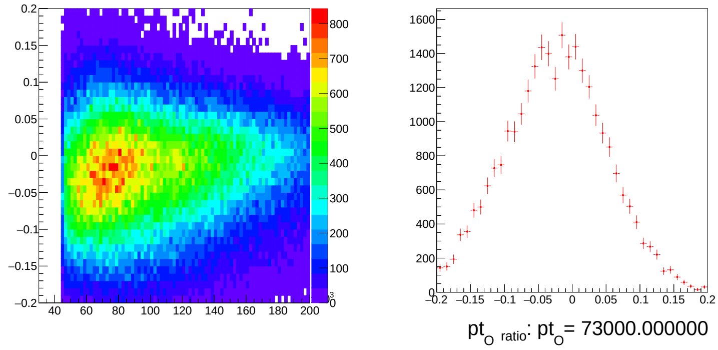

Figure 4.25: $\Delta p_{\mathrm{T}\ ratio}$ for the leading p_{T} non b-jet with $0 < \eta < 1$ from MC events against p_{T} of the offline b-jet. A slice across the y-axis has been taken at $p_{\mathrm{T}} = 79\mathrm{GeV}$.

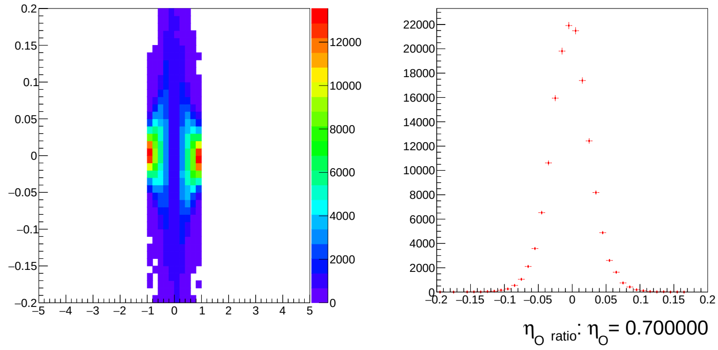

Figure 4.26: $\Delta\eta_{ratio}$ for the leading p_{T} non b-jet with $0 < \eta < 1$ from MC events against η of the offline b-jet. A slice across the y-axis has been taken at $\eta = -1.9$.

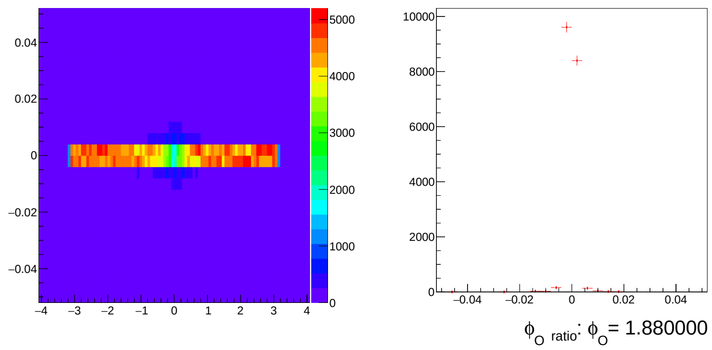

Figure 4.27: $\Delta\phi_{ratio}$ for the leading p_{T} non b-jet with $0 < \eta < 1$ from MC events against ϕ of the offline b-jet. A slice across the y-axis has been taken at $\phi = -1.64$.

4.4 Core

4.4.1 Monte-Carlo

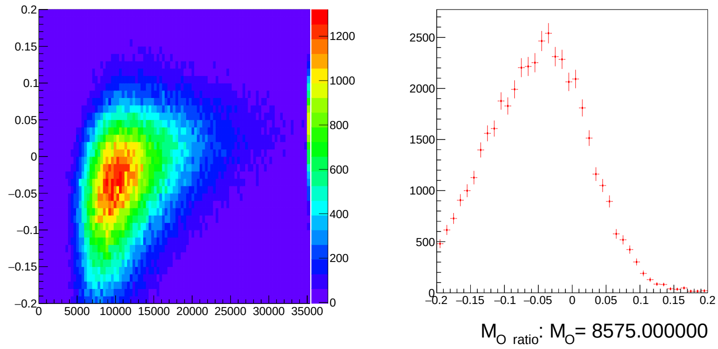

Figure 4.28: ΔM_{ratio} for the leading p_{T} non b-jet with $0 < \eta < 1$ from MC events against M of the offline b-jet. A slice across the y-axis has been taken at $M = 7$GeV.

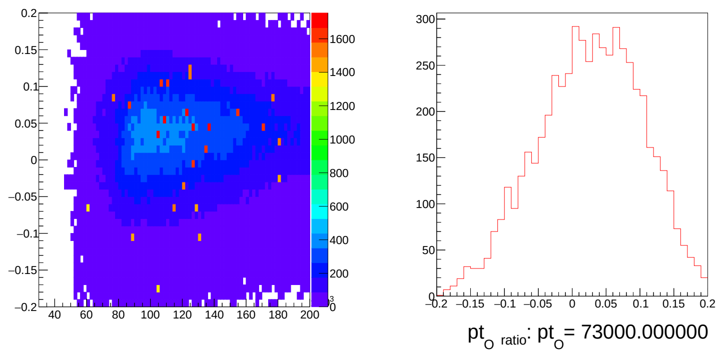

Figure 4.29: $\Delta p_{\mathrm{T}\ ratio}$ for the leading p_{T} non b-jet with $0 < \eta < 1$ from Data events against p_{T} of the offline b-jet. A slice across the y-axis has been taken at $p_{\mathrm{T}} = 79$GeV.

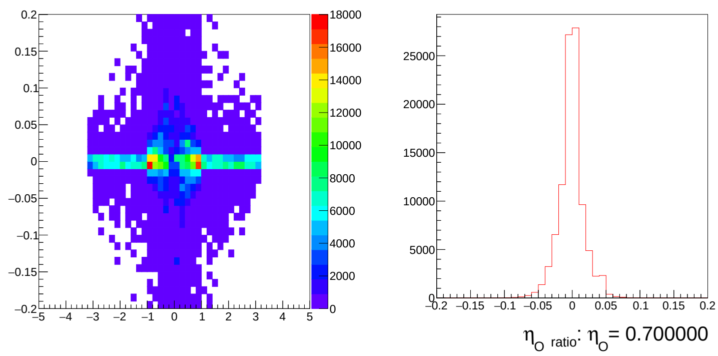

Figure 4.30: $\Delta\eta_{ratio}$ for the leading p_{T} non b-jet with $0 < \eta < 1$ from Data events against η of the offline b-jet. A slice across the y-axis has been taken at $\eta = -1.9$.

4.4.1.1 Data

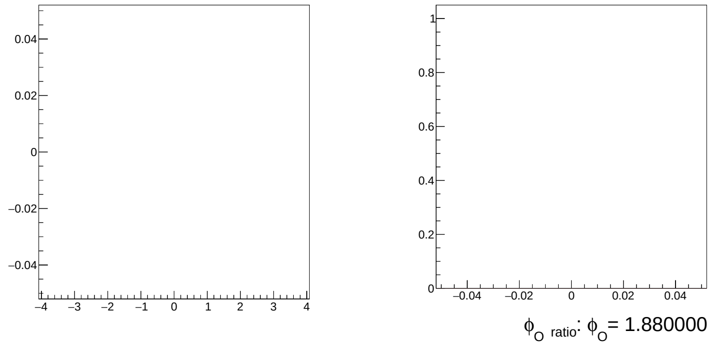

Figure 4.31: $\Delta\phi_{ratio}$ for the leading p_{T} non b-jet with $0 < \eta < 1$ from Data events against ϕ of the offline b-jet. A slice across the y-axis has been taken at $\phi = -1.64$.

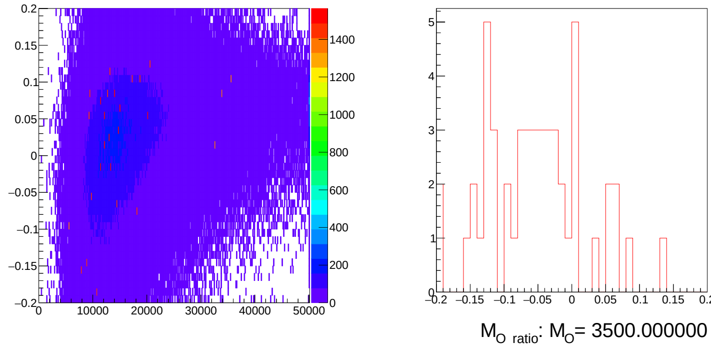

Figure 4.32: ΔM_{ratio} for the leading p_{T} non b-jet with $0 < \eta < 1$ from Data events against M of the offline b-jet. A slice across the y-axis has been taken at $M = 7$GeV.

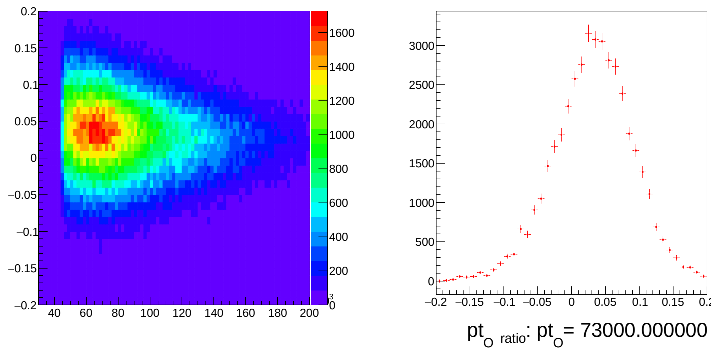

Figure 4.33: $\Delta p_{\mathrm{T}\ ratio}$ for the leading p_{T} b-jet with $1 < \eta < 2.4$ from MC events against p_{T} of the offline b-jet. A slice across the y-axis has been taken at $p_{\mathrm{T}} = 79$GeV.

4.4.2 Non Bjets

4.4.3 Monte-Carlo

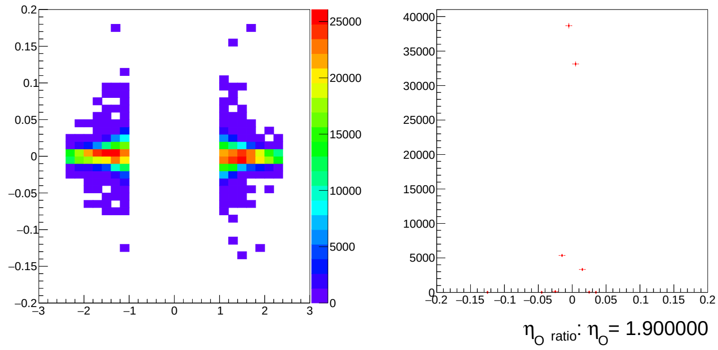

Figure 4.34: $\Delta\eta_{ratio}$ for the leading p_{T} b-jet with $1 < \eta < 2.4$ from MC events against η of the offline b-jet. A slice across the y-axis has been taken at $\eta = -1.9$.

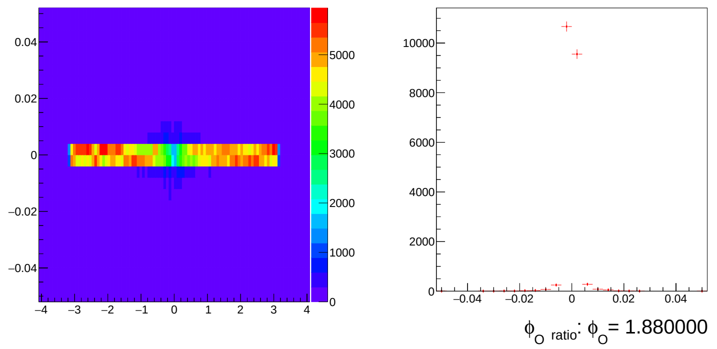

Figure 4.35: $\Delta\phi_{ratio}$ for the leading p_{T} b-jet with $1 < \eta < 2.4$ from MC events against ϕ of the offline b-jet. A slice across the y-axis has been taken at $\phi = -1.64$.

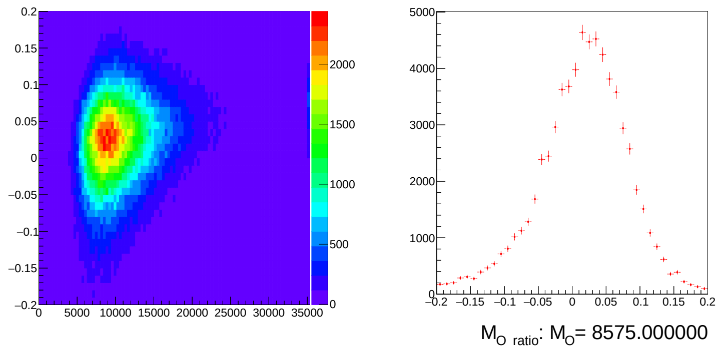

Figure 4.36: ΔM_{ratio} for the leading p_{T} b-jet with $1 < \eta < 2.4$ from MC events against M of the offline b-jet. A slice across the y-axis has been taken at M = 7GeV.

4.4.4 Data

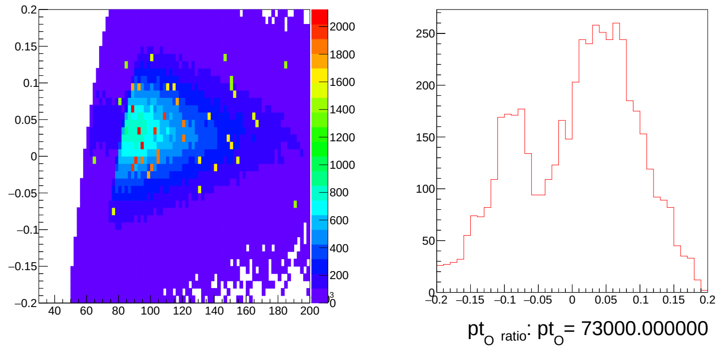

Figure 4.37: $\Delta p_{\mathrm{T}\ ratio}$ for the leading p_{T} b-jet with $1 < \eta < 2.4$ from Data events against p_{T} of the offline b-jet. A slice across the y-axis has been taken at $p_{\mathrm{T}} = 79$GeV.

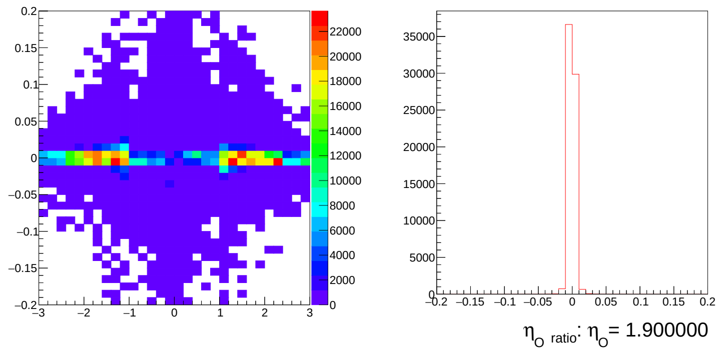

Figure 4.38: $\Delta\eta_{ratio}$ for the leading p_{T} b-jet with $1 < \eta < 2.4$ from Data events against η of the offline b-jet. A slice across the y-axis has been taken at $\eta = -1.9$.

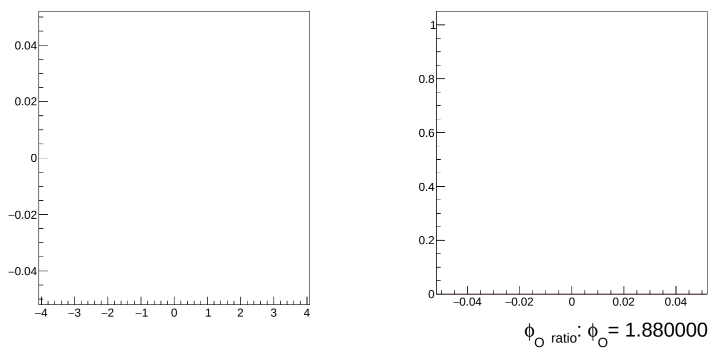

Figure 4.39: $\Delta\phi_{ratio}$ for the leading p_{T} b-jet with $1 < \eta < 2.4$ from Data events against ϕ of the offline b-jet. A slice across the y-axis has been taken at $\phi = -1.64$.

spacing

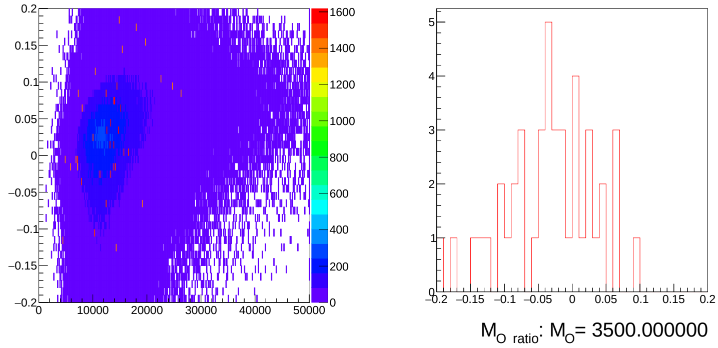

Figure 4.40: ΔM_{ratio} for the leading $p_{\rm T}$ b-jet with $1 < \eta < 2.4$ from Data events against M of the offline b-jet. A slice across the y-axis has been taken at M = 7GeV.

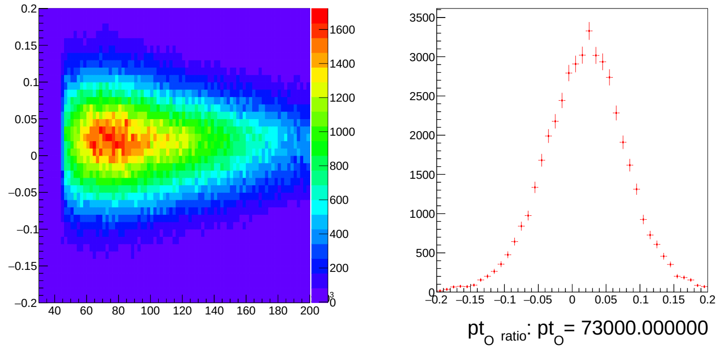

Figure 4.41: $\Delta p_{\rm T\ ratio}$ for the leading $p_{\rm T}$ non b-jet with $1 < \eta < 2.4$ from MC events against $p_{\rm T}$ of the offline b-jet. A slice across the y-axis has been taken at $p_{\rm T}$ = 79GeV.

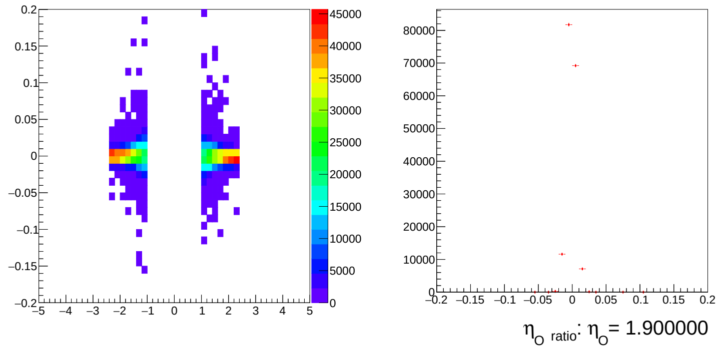

Figure 4.42: $\Delta\eta_{ratio}$ for the leading $p_{\rm T}$ non b-jet with $1 < \eta < 2.4$ from MC events against η of the offline b-jet. A slice across the y-axis has been taken at $\eta = -1.9$.

spacing

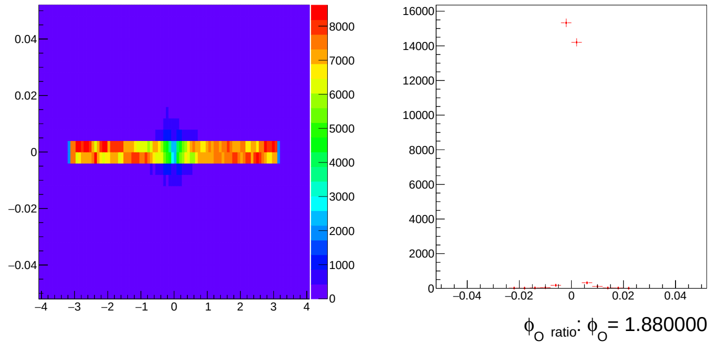

Figure 4.43: $\Delta\phi_{ratio}$ for the leading p_{T} non b-jet with $1 < \eta < 2.4$ from MC events against ϕ of the offline b-jet. A slice across the y-axis has been taken at $\phi = -1.64$.

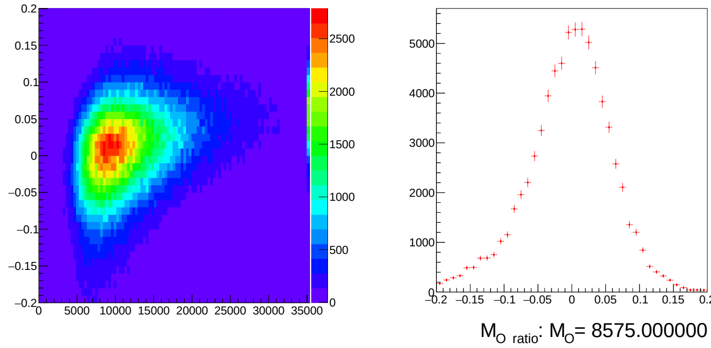

Figure 4.44: ΔM_{ratio} for the leading p_{T} non b-jet with $1 < \eta < 2.4$ from MC events against M of the offline b-jet. A slice across the y-axis has been taken at M = 7GeV.

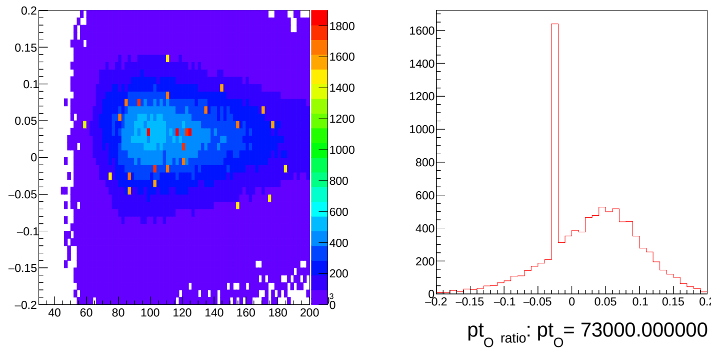

Figure 4.45: $\Delta p_{\mathrm{T}\ ratio}$ for the leading p_{T} non b-jet with $1 < \eta < 2.4$ from Data events against p_{T} of the offline b-jet. A slice across the y-axis has been taken at p_{T} = 79GeV.

4.5 Forward Jets

4.5.1 Monte-Carlo

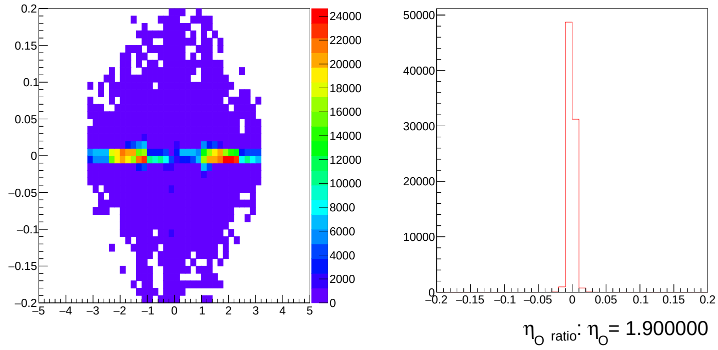

Figure 4.46: $\Delta\eta_{ratio}$ for the leading p_{T} non b-jet with $1 < \eta < 2.4$ from Data events against η of the offline b-jet. A slice across the y-axis has been taken at $\eta = -1.9$.

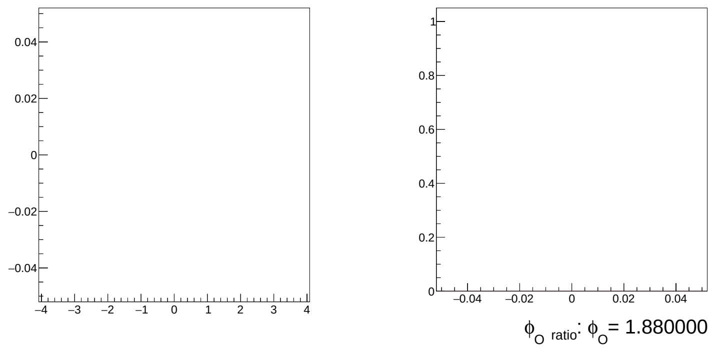

Figure 4.47: $\Delta\phi_{ratio}$ for the leading p_{T} non b-jet with $1 < \eta < 2.4$ from Data events against ϕ of the offline b-jet. A slice across the y-axis has been taken at $\phi = -1.64$.

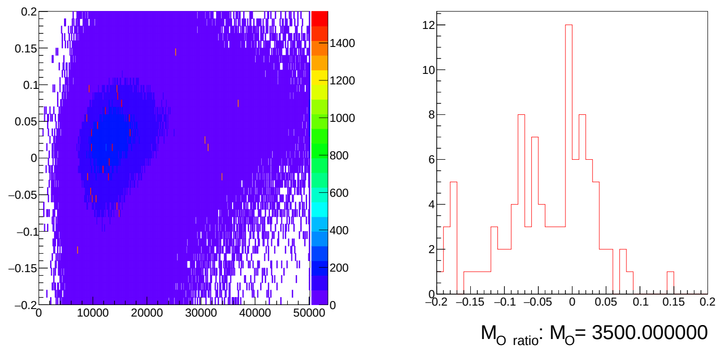

Figure 4.48: ΔM_{ratio} for the leading p_{T} non b-jet with $1 < \eta < 2.4$ from Data events against M of the offline b-jet. A slice across the y-axis has been taken at $M = 7$GeV.

4.5.2 Data

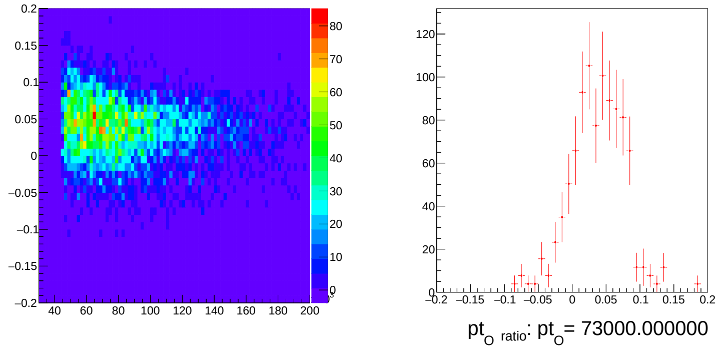

Figure 4.49: $\Delta p_{\mathrm{T}\ ratio}$ for the leading p_{T} b-jet with $2.4 < |\eta|$ from MC events against p_{T} of the offline b-jet. A slice across the y-axis has been taken at $p_{\mathrm{T}} = 79$GeV.

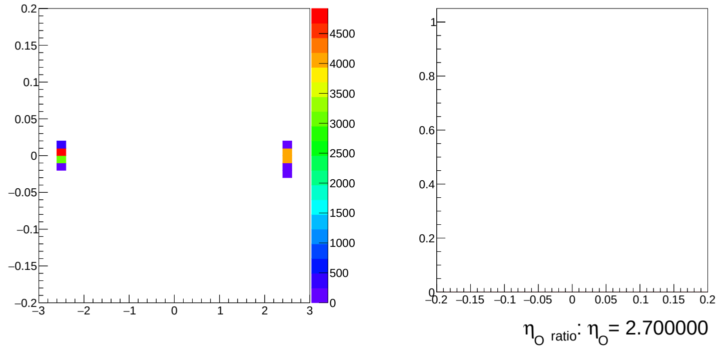

Figure 4.50: $\Delta\eta_{ratio}$ for the leading p_{T} b-jet $2.4 < |\eta|$ from MC events against η of the offline b-jet. A slice across the y-axis has been taken at $\eta = -1.9$.

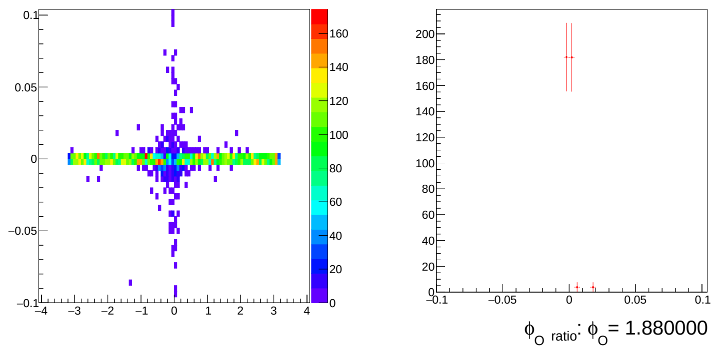

Figure 4.51: $\Delta\phi_{ratio}$ for the leading p_{T} b-jet $2.4 < |\eta|$ from MC events against ϕ of the offline b-jet. A slice across the y-axis has been taken at $\phi = -1.64$.

4.5.3 Non bjets

4.5.4 Monte-Carlo

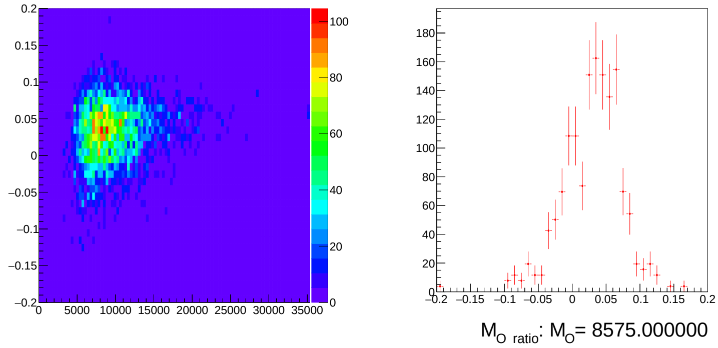

Figure 4.52: ΔM_{ratio} for the leading p_T b-jet $2.4 < |\eta|$ from MC events against M of the offline b-jet. A slice across the y-axis has been taken at $M = 7$GeV.

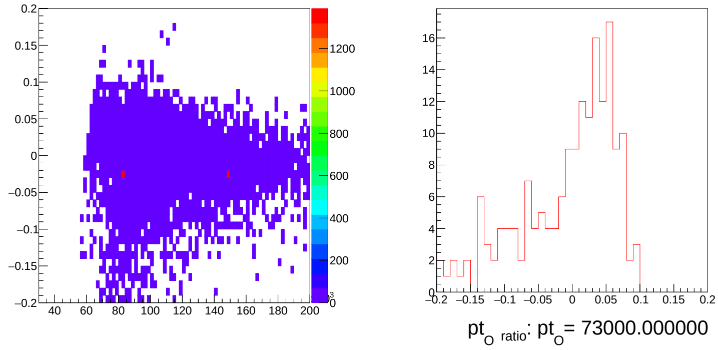

Figure 4.53: $\Delta p_{T\ ratio}$ for the leading p_T b-jet with $2.4 < |\eta|$ from Data events against p_T of the offline b-jet. A slice across the y-axis has been taken at $p_T = 79$GeV.

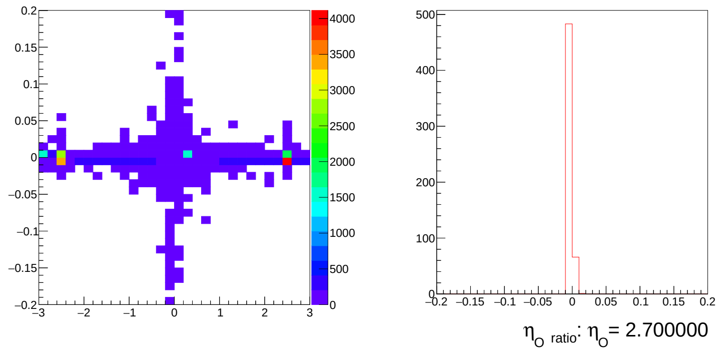

Figure 4.54: $\Delta\eta_{ratio}$ for the leading p_T b-jet $2.4 < |\eta|$ from Data events against η of the offline b-jet. A slice across the y-axis has been taken at $\eta = -1.9$.

4.5.5 Data

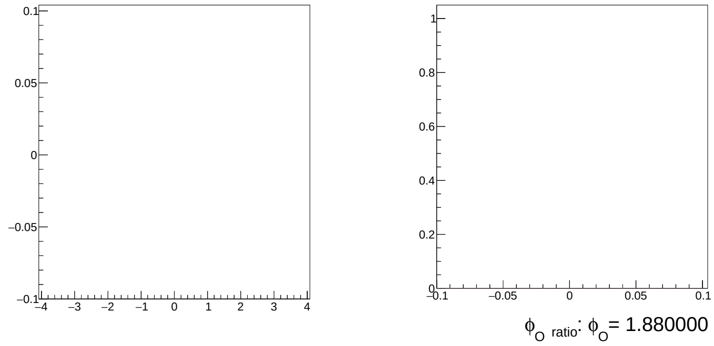

Figure 4.55: $\Delta\phi_{ratio}$ for the leading p_{T} b-jet $2.4 < |\eta|$ from Data events against ϕ of the offline b-jet. A slice across the y-axis has been taken at $\phi = -1.64$.

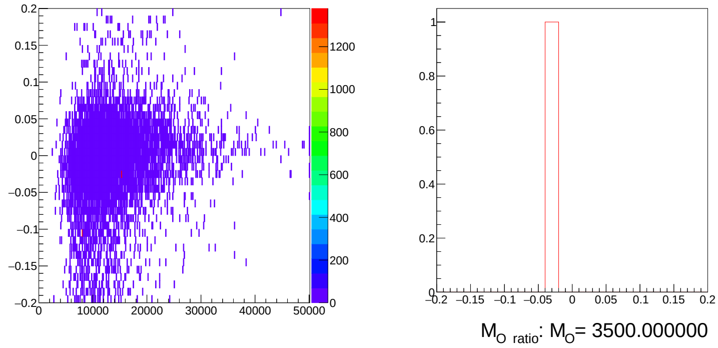

Figure 4.56: ΔM_{ratio} for the leading p_{T} b-jet $2.4 < |\eta|$ from Data events against M of the offline b-jet. A slice across the y-axis has been taken at $M = 7$GeV.

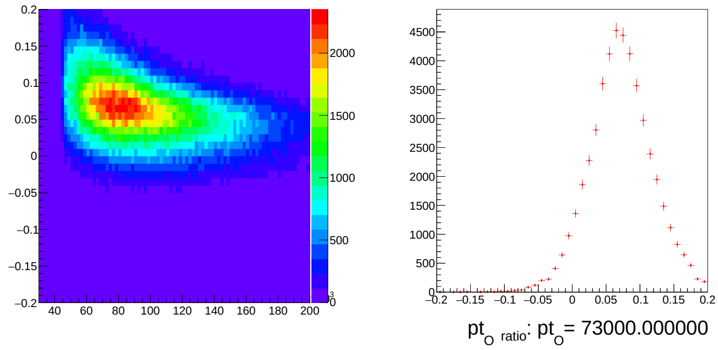

Figure 4.57: $\Delta p_{\mathrm{T}\ ratio}$ for the leading p_{T} non b-jet $2.4 < |\eta|$ from MC events against p_{T} of the offline b-jet. A slice across the y-axis has been taken at $p_{\mathrm{T}} = 79$GeV.

4.6 Jet Tagging Efficiency

As covered in 2.5.1, the standard algorithm for 2016 physics analyses was chosen to be the 2016 MV2c10 algorithm. However, the HLT b-tagging algorithm uses the MV2c20 algorithm. [24] To perform a valid TLA the perfomance of the tagging algorithms between trigger level and

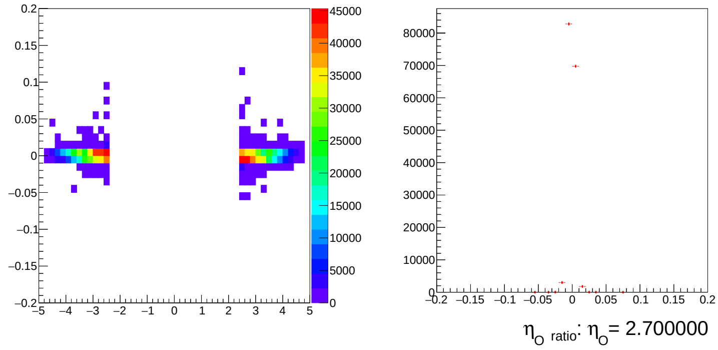

Figure 4.58: $\varDelta\eta_{ratio}$ for the leading p_{T} non b-jet $2.4 < |\eta|$ from MC events against η of the offline b-jet. A slice across the y-axis has been taken at $\eta = -1.9$.

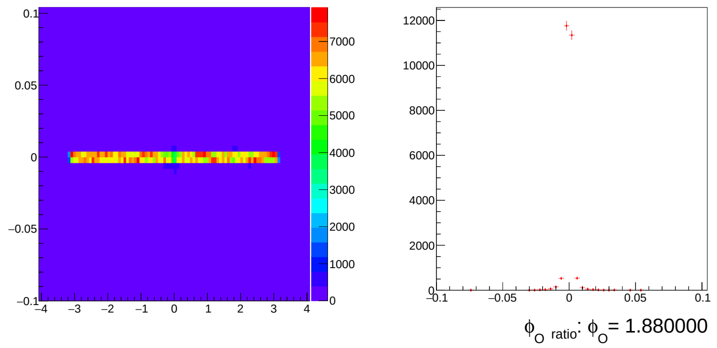

Figure 4.59: $\varDelta\phi_{ratio}$ for the leading p_{T} non b-jet $2.4 < |\eta|$ from MC events against ϕ of the offline b-jet. A slice across the y-axis has been taken at $\phi = -1.64$.

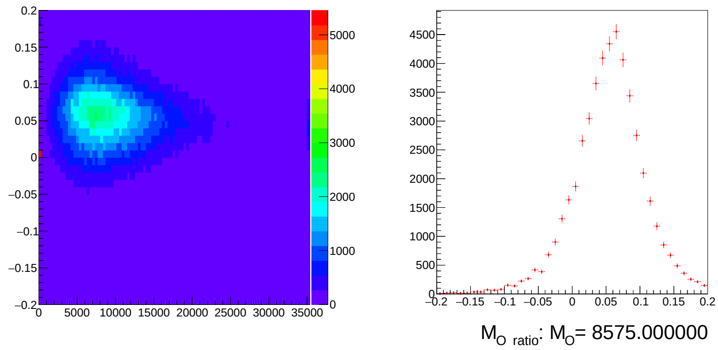

Figure 4.60: $\varDelta M_{ratio}$ for the leading p_{T} non b-jet $2.4 < |\eta|$ from MC events against M of the offline b-jet. A slice across the y-axis has been taken at $M = 7$GeV.

offline must be similar. With the datasets used for this analysis (**??**) the MC data produced in 2015 would make use of the older configurations compared to the newer configurations in the data.

not sure what effect this config changes had on the trigger

Here the tagging efficiency of the HLT and offline taggers is studied for different jet flavours in the MC sample. An offline/HLT jet pair was formed using $\varDelta R$ matching and truth label of

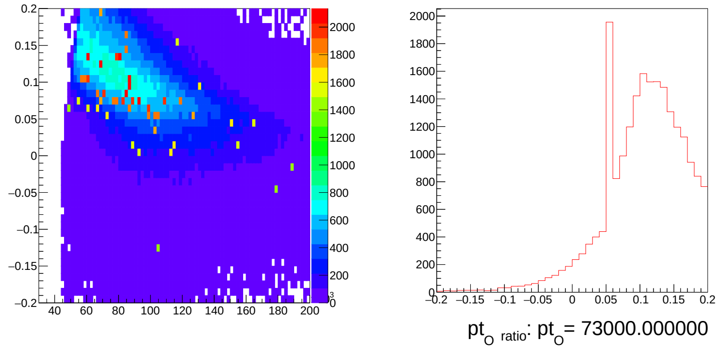

Figure 4.61: $\Delta p_{\mathrm{T}\ ratio}$ for the leading p_{T} non b-jet $2.4 < |\eta|$ from Data events against p_{T} of the offline b-jet. A slice across the y-axis has been taken at p_{T} = 79GeV.

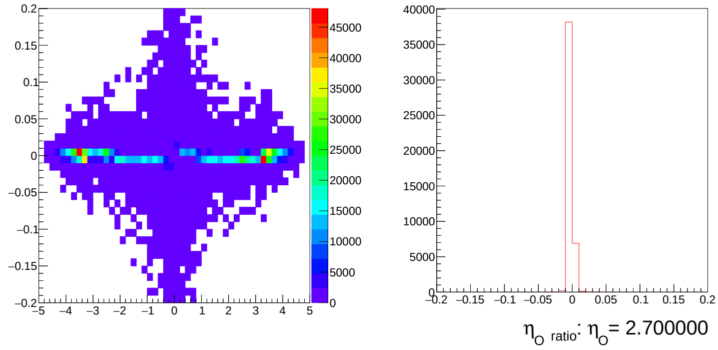

Figure 4.62: $\Delta\eta_{ratio}$ for the leading p_{T} non b-jet $2.4 < |\eta|$ from Data events against η of the offline b-jet. A slice across the y-axis has been taken at $\eta = -1.9$.

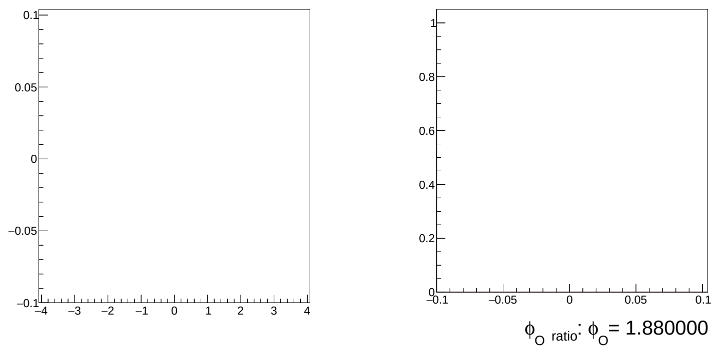

Figure 4.63: $\Delta\phi_{ratio}$ for the leading p_{T} non b-jet $2.4 < |\eta|$ from Data events against ϕ of the offline b-jet. A slice across the y-axis has been taken at $\phi = -1.64$.

the jet used to assign a flavour. The efficiency plots in figures 4.65, 4.66 and 4.67 show the fraction of these jets that were identified as b-jets by the HLT and offline tagging algorithms.

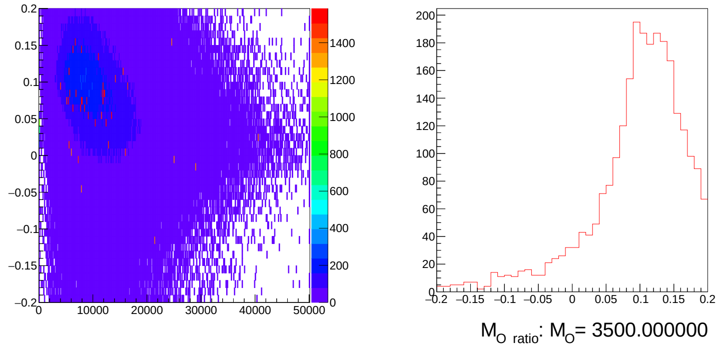

Figure 4.64: ΔM_{ratio} for the leading p_{T} non b-jet $2.4 < |\eta|$ from Data events against M of the offline b-jet. A slice across the y-axis has been taken at $M = 7$GeV.

4.6.1 *b*-jet efficiency

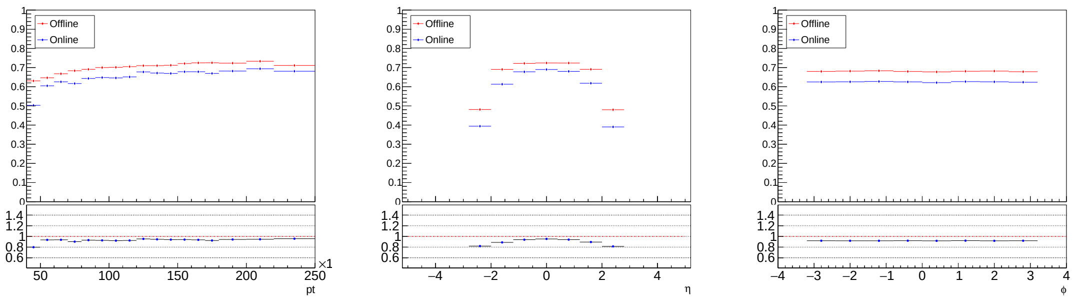

Figure 4.65:

To do: Options, could show more vars or alternatively the reference hists, or alternatively just reference the references

4.6.2 *c*-jet efficiency

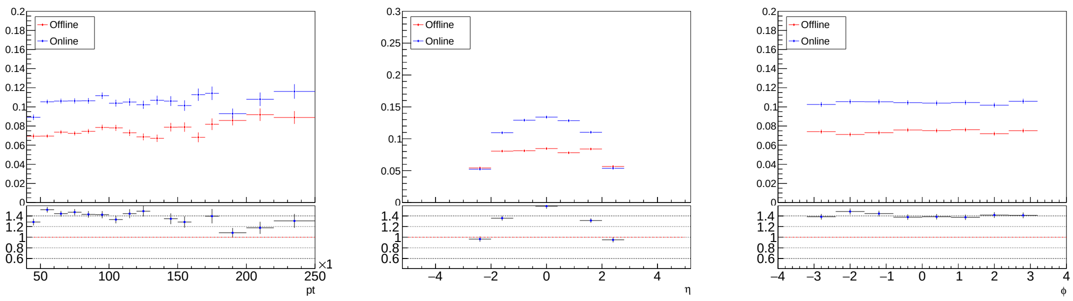

Figure 4.66:

4.6.3 Light-jet efficiency

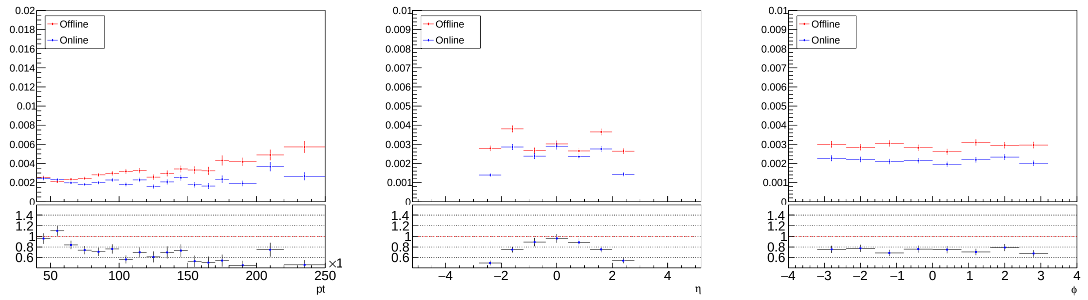

Figure 4.67:

4.6.4 Tag Matching

For each pair of jets that could be matched between online and offline, and then successfully have a b-tagging decision evaluated on the jets, the agreement of the b-tagging between the two jets was checked. These were found to match one another in 90.91% of cases.

4.6.5 Comparison of HLT and offline tagging efficiencies

Primarily considering the p_T plots of efficiency, the HLT b-tagging is found to be around 5% less efficient than the offline b-tagging for jets with $p_T > 50$GeV. This is a consistent direction of efficiency shift as found when comparing the 2016 MV2c10 and 2015 MV2c20 algorithms on the training $t\bar{t}$ sample, but of a larger magnitude. The increase in the rate of c-jet mistagging is absolutely consitent with the refinements to the algorithm between the 2016 MV2c10 and 2015 MV2c20, with increased levels of c-jet rejection in the offline 2016 MV2c10, and the $\sim$ 40% increase is consistent with the expected shift from the optimised algorithm. [26] The light-jet behaviour is also similar as expected but ????.

To do: some light jet related shenanigans

4.7 MV2 Discriminant Values - ???

To do: Necessary

Here would show plots of the MV2 value against pt/eta or whatever

CHAPTER 5

KINEMATICS

5.1 Specific Jet Feature Distributions

For the standard set of jet features, plot the overall distributions in a standard 2 hist ratio plot for data and MC. This also includes jet counts possibly

5.2 Specific Jet Feature Distributions

5.2.1 Two Central Channel

5.2.1.1 p_{T}

5.2.1.2 η

5.2.1.3 ϕ

5.2.1.4 M

5.3 BDT Input Variables

- M_{jj}
- $p_{\mathrm{T}\ jj}$
- $\cos\theta$
- $\Delta\eta_{jj}$
- $Max(\eta)$
- $\eta*$

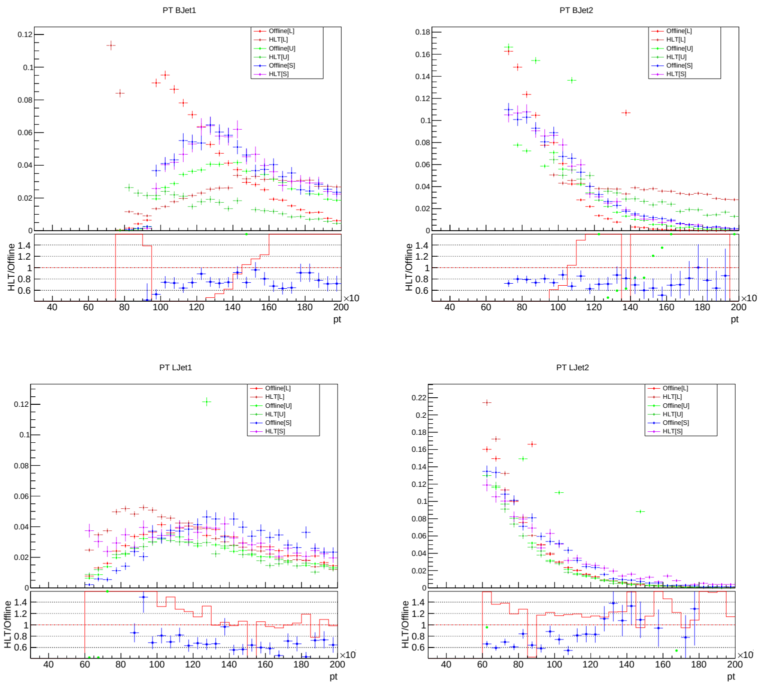

- $min\mathit{\Delta}R(j_1)$
- $min\mathit{\Delta}R(j_1)$
- p_{T} balance
- $N_{TRK}(j_1)PV500$?
- $N_{TRK}(j_{})PV500$?

5.4 Mbb Distribution

Prior paper suggests this is the 'final' plot, a shape comparison between BDT influenced control and signal regions of the Mbb distribution. A little confused as to exactly what we need here.

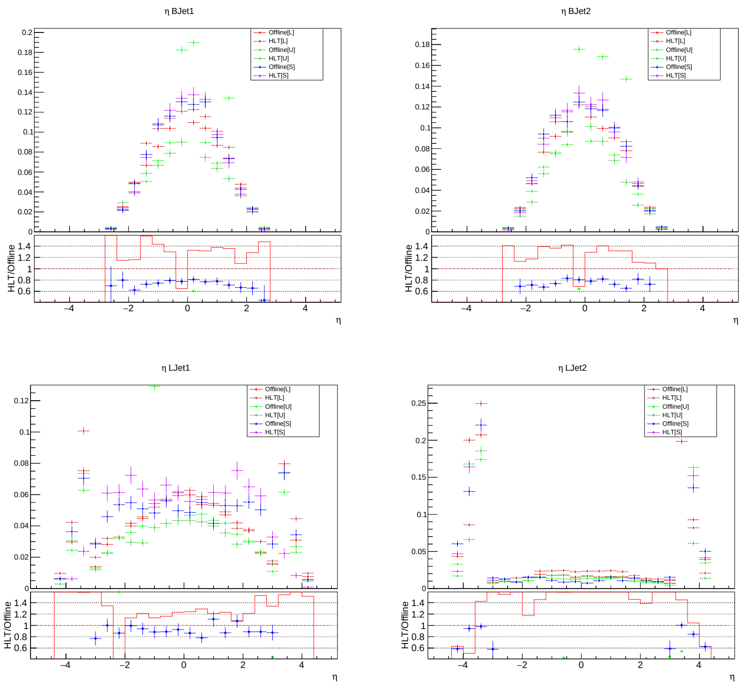
η BJet1
η BJet2
η LJet1
η LJet2
Offline[L]
HLT[L]
Offline[U]
HLT[U]
Offline[S]
HLT[S]
HLT/Offline
η

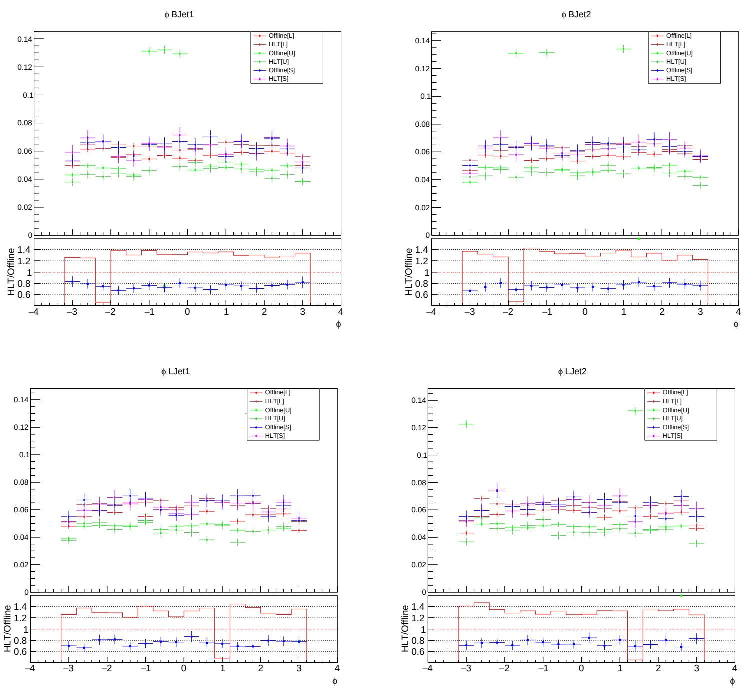
ϕ BJet1
ϕ BJet2
ϕ LJet1
ϕ LJet2
Offline[L]
HLT[L]
Offline[U]
HLT[U]
Offline[S]
HLT[S]
HLT/Offline
ϕ

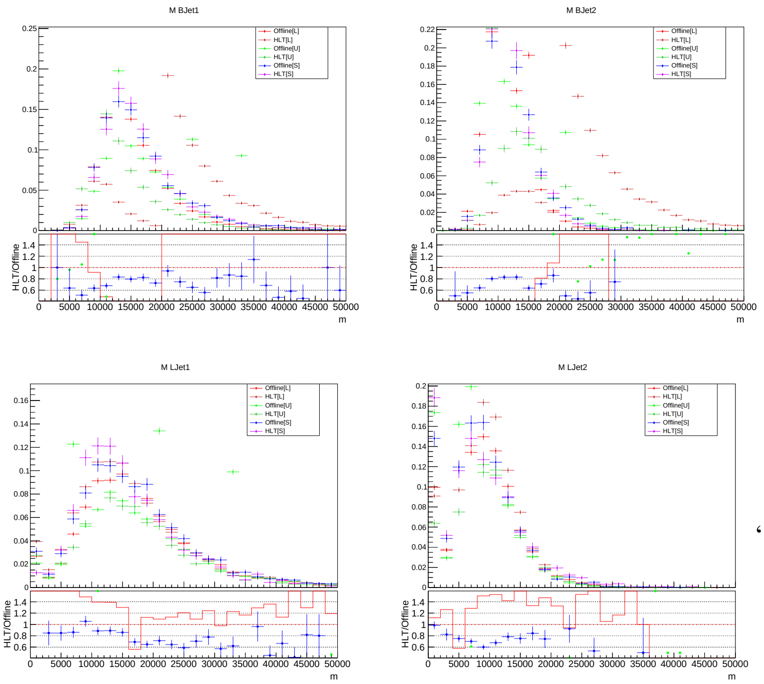

1

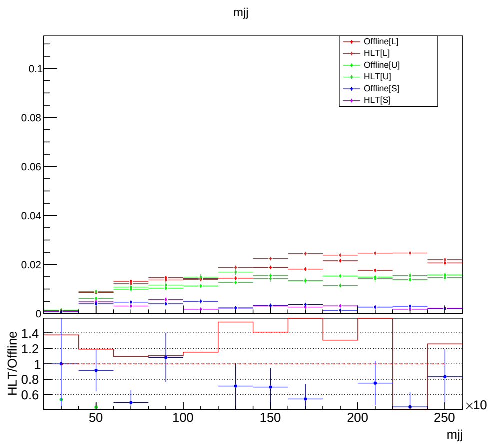

Figure 5.1:

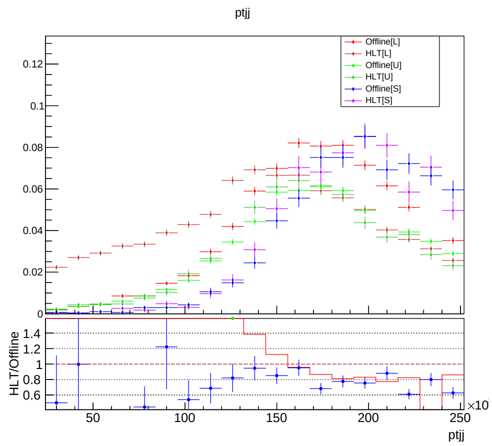

Figure 5.2:

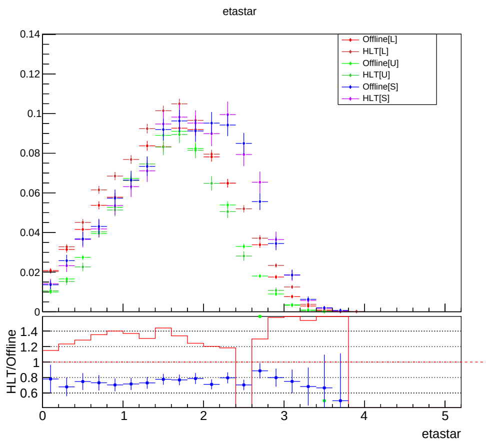

Figure 5.3:

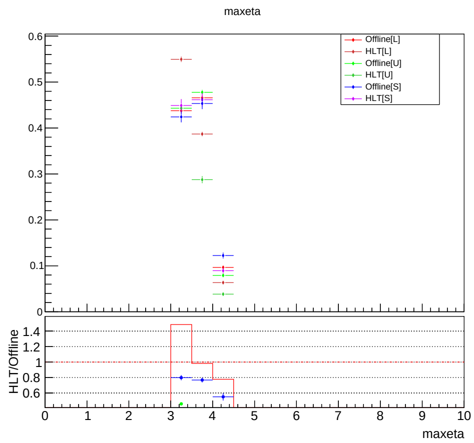

Figure 5.4:

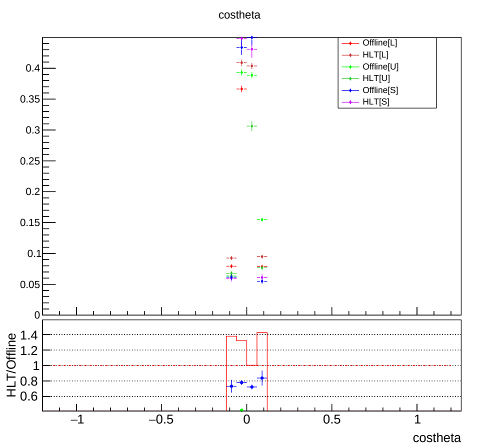

Figure 5.5:

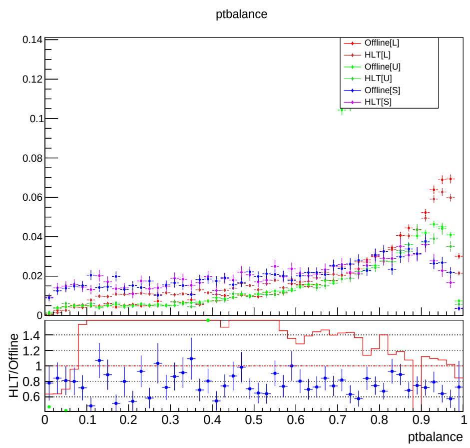

Figure 5.6:

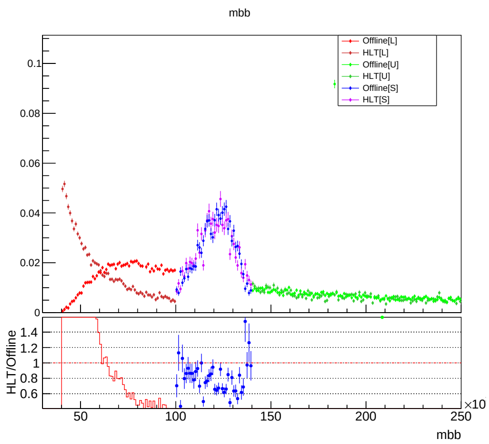

Figure 5.7:

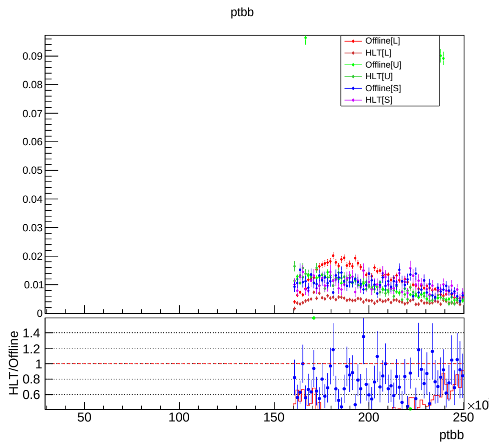

Figure 5.8:

Bibliography

[1] Particle Data Group Collaboration, C. Patrignani et al., *Review of Particle Physics*, Chin. Phys. **C40** no. 10, (2016) 100001.

[2] F. Englert and R. Brout, *Broken Symmetry and the Mass of Gauge Vector Mesons*, Phys. Rev. Lett. **13** (1964) 321–323.

[3] P. W. Higgs, *Broken Symmetries and the Masses of Gauge Bosons*, Phys. Rev. Lett. **13** (1964) 508–509.

[4] P. W. Higgs, *Broken symmetries, massless particles and gauge fields*, Phys. Lett. **12** (1964) 132–133.

[5] S. L. Glashow, *Partial Symmetries of Weak Interactions*, Nucl. Phys. **22** (1961) 579–588.

[6] S. Weinberg, *A Model of Leptons*, Phys. Rev. Lett. **19** (1967) 1264–1266.

[7] A. Salam, *Weak and Electromagnetic Interactions*, Conf. Proc. **C680519** (1968) 367–377.

[8] N. Cabibbo, *Unitary Symmetry and Leptonic Decays*, Phys. Rev. Lett. **10** (1963) 531–533. [,648(1963)].

[9] M. Kobayashi and T. Maskawa, *CP Violation in the Renormalizable Theory of Weak Interaction*, Prog. Theor. Phys. **49** (1973) 652–657.

[10] ATLAS Collaboration, G. Aad et al., *Observation of a new particle in the search for the Standard Model Higgs boson with the ATLAS detector at the LHC*, Phys. Lett. **B716** (2012) 1–29, `arXiv:1207.7214 [hep-ex]`.

[11] CMS Collaboration, S. Chatrchyan et al., *Observation of a new boson at a mass of 125 GeV with the CMS experiment at the LHC*, Phys. Lett. **B716** (2012) 30–61, `arXiv:1207.7235 [hep-ex]`.

[12] NNPDF Collaboration, R. D. Ball et al., *Parton distributions for the LHC Run II*, JHEP **04** (2015) 040, `arXiv:1410.8849 [hep-ph]`.

[13] J. C. Collins, *Light cone variables, rapidity and all that*, `arXiv:hep-ph/9705393 [hep-ph]`.

[14] M. H. Seymour and M. Marx, *Monte Carlo Event Generators*, pp. , 287–319. 2013. arXiv:1304.6677 [hep-ph]. https://inspirehep.net/record/1229804/files/arXiv:1304.6677.pdf.

[15] LHC Higgs Cross Section Working Group Collaboration, S. Dittmaier et al., *Handbook of LHC Higgs Cross Sections: 1. Inclusive Observables*, arXiv:1101.0593 [hep-ph].

[16] S. Asai et al., *Prospects for the search for a standard model Higgs boson in ATLAS using vector boson fusion*, Eur. Phys. J. **C32S2** (2004) 19–54, arXiv:hep-ph/0402254 [hep-ph].

[17] LHC Higgs Cross Section Working Group Collaboration, J. R. Andersen et al., *Handbook of LHC Higgs Cross Sections: 3. Higgs Properties*, arXiv:1307.1347 [hep-ph].

[18] L. Evans and P. Bryant, *LHC Machine*, JINST **3** (2008) S08001.

[19] *LEP design report*. CERN, Geneva, 1983. https://cds.cern.ch/record/98881. By the LEP Injector Study Group.

[20] *LEP design report*. CERN, Geneva, 1984. https://cds.cern.ch/record/102083. Copies shelved as reports in LEP, PS and SPS libraries.

[21] Y. Koshiba et al., *Luminosity Increase in Laser-Compton Scattering by Crab Crossing Method*, in *Proc. of International Particle Accelerator Conference (IPAC'17), Copenhagen, Denmark, 14ÃćÂĂŞ19 May, 2017*, pp. , 902–904. JACoW, Geneva, Switzerland, May, 2017. http://jacow.org/ipac2017/papers/mopva023.pdf. https://doi.org/10.18429/JACoW-IPAC2017-MOPVA023.

[22] ATLAS Collaboration, G. Aad et al., *The ATLAS Experiment at the CERN Large Hadron Collider*, JINST **3** (2008) S08003.

[23] J. Pequenao, "Computer generated image of the whole ATLAS detector." https://cds.cern.ch/record/1095924. Accessed 03/09/2017.

[24] ATLAS Collaboration, M. Aaboud et al., *Performance of the ATLAS Trigger System in 2015*, Eur. Phys. J. **C77** no. 5, (2017) 317, arXiv:1611.09661 [hep-ex].

[25] R. Achenbach et al., *The ATLAS level-1 calorimeter trigger*, JINST **3** (2008) P03001.

[26] ATLAS Collaboration, *Optimisation of the ATLAS b-tagging performance for the 2016 LHC Run*, ATL-PHYS-PUB-2016-012 (2016). https://cds.cern.ch/record/2160731.

[27] ATLAS Collaboration, *Performance of b-Jet Identification in the ATLAS Experiment*, JINST **11** no. 04, (2016) P04008, arXiv:1512.01094 [hep-ex].